https://doi.org/10.5194/amt-2019-81
Preprint. Discussion started: 3 June 2019

Atmospheric Measurement Techniques Discussions

A Fast Visible Wavelength 3-D Radiative Transfer Procedure for NWP Visualization and Forward Modeling

Steven Albers[1], Stephen M. Saleeby[2], Sonia Kreidenweis[2], Qijing Bian[2], Peng Xian[3], Zoltan Toth[4], Ravan Ahmadov[5,4], Eric James[5,4], and Steven D. Miller[2]

1 - Spire Global, Inc., Boulder, CO
2 - Colorado State University, Ft. Collins, CO
3 - U.S. Naval Research Laboratory, Monterey, CA
4 - Global Systems Division, ESRL/OAR/NOAA,
5 - CIRES at Global Systems Division, ESRL/OAR/NOAA

Abstract:

Solar radiation is the ultimate source of energy for all atmospheric motions. The visible wavelength range of solar radiation represents a significant contribution to the Earth's energy budget and visible light is a vital indicator for the composition and thermodynamic processes of the atmosphere from the smallest weather to the largest climate scales. The accurate and fast description of light propagation in the atmosphere and its lower boundary environment is therefore of critical importance for the simulation and prediction of weather and climate.

Simulated Weather Imagery (SWIm) is a new, fast and physically based visible wavelength 3-dimensional radiative transfer model. Given the location and intensity of the sources of light (natural or artificial) and the composition (e.g., clear or turbid air with aerosols, liquid or ice clouds, and precipitating rain, snow, or ice hydrometeors) of the atmosphere, it describes the propagation of light and produces visually and physically realistic hemispheric or 360° spherical panoramic color images of the atmosphere and the underlying terrain from any specified vantage point either on or above the Earth's surface.

Applications of SWIm include the visualization of atmospheric and land surface conditions simulated or forecast by numerical weather or climate analysis and prediction systems for either scientific or lay audiences. Simulated SWim imagery can also be generated for and compared with observed camera images to (i) assess the fidelity, (ii) and improve the performance of numerical atmospheric and land surface models, as well as (iii) through their inclusion into an observational data assimilation scheme, improve the estimate of the state of atmospheric and land surface initial conditions for situational awareness and NWP forecast initialization applications.

https://doi.org/10.5194/amt-2019-81
Preprint. Discussion started: 3 June 2019

1. Introduction and Motivation

Numerical Weather Prediction (NWP) modeling is a maturing technology for the monitoring and prediction of weather and climate conditions on a wide continuum of timescales (e.g., Kalnay 2003). In NWP models, the large scale variability of the atmosphere is represented via carefully chosen and geographically systematically laid out prognostic variables such as vertically stacked latitude/longitude grids of surface pressure, temperature, wind, humidity, suspended (clouds) and falling (precipitating) hydrometeors, aerosol, etc. Using differential equations, NWP models capture temporal relationships among the atmospheric variables, allowing for the projection of the state of the atmosphere into the future. Short range NWP forecasts (called "first guess") can then be combined with the latest observations of atmospheric conditions to estimate the instantaneous weather conditions at any point in time (called analyzed state, analysis, or forecast initial condition), using Data Assimilation methods (DA, e.g. Kalnay, 2003).

The initialization of forecasts (and thus DA) plays a critical role in NWP as the more complete the information the analysis state has about the atmosphere, the longer pursuant forecasts will retain skill (e.g. Toth and Buizza, 2018). Hence the desire for DA to exploit as many observations, and from as diverse a set of instruments as possible. Some observations are in the form of model variables, in which case, after temporal and/or spatial interpolations, they can be directly combined with a model first guess (i.e., "direct" measurements or observations). Many other instruments, however, observe quantities that are different but can be related to the model variables (i.e., "indirect" measurements).

Indirect observations in the form of visible wavelength light intensity such as those from high (down to 30 second time frequency and 500m pixel) resolution imagers aboard a family of geostationary satellites (e.g., Himawari, GOES-R Advanced Baseline Imager, ABI, Schmit et al., 2017), and from airborne or ground-based cameras offer unique opportunities. First, unlike most other observations, light intensity is readily convertible to color imagery, offering a visual representation of the environment to both specialized (researchers or forecasters) and lay (the general public) users. Note that by far, visual perception is humans' most informative sense. Secondly, high resolution color imagery provides a unique window into fine-scale land surface, aerosol, and cloud processes that are critical both for the monitoring and nowcasting of convective and other severe weather events, as well as for the assessment and refinement of modeled energy balance relationships crucial for climate forecasting.

https://doi.org/10.5194/amt-2019-81
Preprint. Discussion started: 3 June 2019

Atmospheric Measurement Techniques Discussions

Information on related processes derivable from currently available other types of observations is limited in spatiotemporal and other aspects compared to color imagery.

Physically, color imagery is a visual representation of the intensity of different wavelength light (i.e. spectral radiance) reaching a selected point (i.e., location of a photographic or imaging instrument) from an array of directions determined by the design of the instrument, at a given time. For computational efficiency, radiative processes are vastly simplified in NWP models and typically resolve (Sun to atmospheric or land surface gridpoint) only how solar insolation, in a one dimensional manner, affects the temperature conditions in the atmosphere and on the land surface.

Color imagery clearly reflects (no pun intended) the geographical distribution and physical characteristics of cloud, aerosol, and land surface conditions in the natural environment. Some of the related quantities used in NWP models to represent such conditions include the amount of moisture, various forms of cloud forming and falling hydrometeors, the amount and type of aerosols, as well as the amount and type of vegetation and snow cover, and water surface wave characteristics on the ground. Light processes recorded in color imagery constitute indirect measurements of such natural process that before their possible use in the initialization of NWP models, must be quantitatively connected with NWP model prognostic variables.

In the assimilation of direct observations, the value of model variables in the first guess is adjusted toward that of observations (based on the expected level of error in each, (e.g. Kalnay, 2003). In the first step of assimilating indirect observations, simple models (called “forward” models or operators) are used to create “synthetic” observations based on model variables. Synthetic observations simulate what measurements we would get had instruments been placed in the abstract world of an NWP first guess forecast. The model-based synthetic observations then can be compared with real-world measurements of the same (non-model) quantities. Utilizing an adjoint, or ensemble-based inverse of the forward operator, or other minimization procedure, the first guess forecast variables are then adjusted to minimize the difference between the simulated and real observations. In case of visible light measurements, observations can be considered to be in the form of color (or multi-spectral visible) imagery.

It is important to point out that beyond DA applications, the simulation of color imagery from model variables via forward operators has another important purpose.

https://doi.org/10.5194/amt-2019-81
Preprint. Discussion started: 3 June 2019

Atmospheric Measurement Techniques Discussions

This is the visualization of 4D NWP analysis and forecast fields (3 dimensions in space and one across model variables), making such complex data, as pointed out above, readily absorbable by both expert and lay audiences.

Section 2 is a brief review of the general properties and limitations of currently available multispectral radiance and color imagery forward operators. The main contribution of this paper is the introduction of the recently developed fast color imagery forward (or color visible radiation transfer) model called Simulated Weather Imagery (SWIm, Section 3). Section 4 explores two application areas for SWIm: the visualization and validation of NWP analysis and forecast fields, as well as a vision for the assimilation of color imagery observations into NWP analysis fields. Closing remarks and some discussion are offered in Section 5.

2. Color Imagery and Spectral Radiance Forward Modeling

Light observations used in color imagery are affected by three main factors: (1) the light source (its location and intensity across the visible spectrum); (2) the medium through which the light travels (the composition and density of its constituents in 3D space); and (3) the location where the light is observed or perceived (Fig. 2). Conceptually, how light from a given source would propagate through a medium and affect an instrument or receptor involves a realistic (a) relative placement of the light source, medium, and receptor with respect to each other (prescribed); (b) representation of light emission from its source (prescribed); (c) description of the medium (from an NWP analysis of the atmosphere and its surroundings); (d) simulation of how light is modified as it travels through the medium via absorptive and diffusive processes; and (e) simulation of the response of the instrument or human observer to the natural stimuli. Full, end-to-end color imagery forward modeling involves the specification of (a) and (b), and based on the conditions of the medium estimated in (c), the simulation of processes described in (d) ("ray-tracing"), as well as the consideration of the impact of radiation (e).

Light propagation has been extensively studied from both experimental and theoretical perspectives. The scientifically most rigorous treatment involves the study of how individual photons are affected by, and a stochastic analysis of, the expected or net effect of scattering and absorption. Named after the stochastic concept involved, this line of inquiry and the related methodology is called the "Monte Carlo" approach. As seen from figure 1, the Monte Carlo approach (M*ayer,* 2009) works in a wide variety of situations with the 3-D fields, arbitrary vantage points, and day/night applications. Figure 1 also lists the characteristics of some other widely used radiative

https://doi.org/10.5194/amt-2019-81
Preprint. Discussion started: 3 June 2019

Atmospheric Measurement Techniques Discussions

transfer models. Whereas the Monte Carlo (MC) model is physically more rigorous, it is computationally much more intensive than some of the other methods. The computational efficiency of the other methods come at a cost of significant approximations or other limitations. For example, the Rapid Radiative Transfer Model (RRTM) provides irradiance at different grid levels and is used as a radiation parameterization package in NWP models. As typical for such packages, RRTM operates in single columns, hence it cannot produce 3-D directional imagery that the Monte Carlo approach can. The Community Radiative Transfer Model (CRTM, Kleespies et al., 2004) is used for both visualization and as a radiative forward operator in variational and related DA systems. The Spherical Discrete Harmonic Ordinate Method (SHDOM, Evans, 1998, Doicu et al., 2013) is another sophisticated radiative transfer model often used in fine scale research studies. SHDOM can produce imagery with good physical accuracy.

Figure 1 also lists the characteristics of SWIm, the recently developed method that the next section describes in some detail. SWIm was designed for the production of color imagery under a wide range of conditions. To satisfy such a requirement, approximations to the more rigorous treatment of some physical processes had to be made. The level of approximations was carefully chosen to improve computational efficiency without unnecessarily sacrificing accuracy. By considering human color vision perception, SWIm can also produce images that are visually realistic. This is a unique feature that allows the simulated images to be directly compared with photographic color images since it can accurately convert spectral radiance values into appropriate displayed RGB values on a computer monitor. As discussed in the rest of this study, with these features SWIm occupies a niche for the versatile visualization and validation of NWP analyses and forecasts, as well as in the assimilation of color imagery observations aimed at the improved initialization of NWP forecasts.

3. Ray Tracing Methodology

SWIm considers the sun in the daytime and the moon at night (if it is sufficiently bright) as nearly point light sources. Information on the medium through which light travels is obtained from 3-D NWP analysis and forecast hydrometeor and aerosol fields. To simulate the propagation of light, SWIm invokes an efficient simplified ray tracing approach that can be benchmarked against results from more sophisticated radiative transfer packages, including the Monte Carlo method. There are two main stages of ray tracing for scattering and absorption calculations. The first is from the sun and the second is from the observer, making SWIm a forward-backward ray-tracing procedure (see FIg. 2). These traces are done on the model grid for the gas, aerosol, and hydrometeor components. Since the actual atmosphere extends above and laterally outside the model grid, an additional separate and faster ray-tracing step is done that considers just the gas and horizontally uniform aerosol components beyond the limited model domain. An algorithmic procedure then combines these results to arrive at the final radiance values and corresponding image display. The above steps are summarized in Table 1 below.

Step 1a: Forward rays from sun (in 3-D grid, including hydrometeors)
Step 1b: Backward rays from observer (in 3-D grid, including hydrometeors)
Step 2: Rays from sun and from observer (in clear air, extending beyond model grid)
Step 3: Combination of radiance components, generate RGB image display.

Table 1. List of ray tracing steps used in SWIm. Steps 1a and 1b are illustrated in Fig. 2.

For gas and aerosols, we evaluate the optical depth, τ, to determine transmittance T, where $T = \frac{I}{Io} = e^{-\tau}$. τ is the number of mean free paths. Io is the initial intensity of the light beam and I is the attenuated intensity. The extinction coefficient α is integrated along the beam path to yield the optical depth. Thus

$$\frac{d\tau}{ds} = \alpha \tag{1}$$

where ds is a distance increment traveling along the light ray and

$$\tau = \int \alpha \, ds \tag{2}$$

The initial forward ray-tracing (step 1a) from the sun through the 3-D grid is tantamount to applying a radiative transfer algorithm to produce a 3-D short wave radiation field. This step is shown as the yellow rays in Fig. 2. We obtain 3-D hydrometeor and aerosol fields from either the analysis (00-hour forecast), or forecast (after the 00-hour initialization). For visually realistic color imagery generation, ray-tracing is done multi-spectrally in three wavelength bands corresponding to the primary colors of human vision and display devices: 615nm (Red), 546nm (Green) and 450nm (Blue). The calculated radiances are represented in the software using an internal variable that is scaled to the solar spectral radiance at the top of the

https://doi.org/10.5194/amt-2019-81
Preprint. Discussion started: 3 June 2019

atmosphere. The light source is the sun in the daytime with the moon being used at night if it is sufficiently bright.

3.1 Solar irradiance and radiance

The top of atmosphere (TOA) solar irradiance E at normal incidence is given by $\frac{1362\ W/m^2}{r^2}$ where r is the Sun-Earth distance in astronomical units. This TOA irradiance can be expressed in terms of spectral irradiance E_λ by considering the solar spectrum in units of W/m^2/nm. We can consider the SWIm image output in the form of spectral radiance L_λ in the spherical image space. L_λ corresponds to surface brightness and customarily is represented in units of W/m^2/sr/nm. For numerical convenience the spectral radiance can be normalized to be in solar relative units based on the TOA solar spectral irradiance, distributed in a hypothetical uniform fashion over the spherical image space having an extent of 4π steradians. We will denote solar normalized (or relative) spectral radiance using the symbol $L_\lambda^{'}$. Thus

$$L_\lambda = L_\lambda^{'} \frac{E_\lambda}{4\pi} \tag{3}$$

and

$$L_\lambda^{'} = \frac{4\pi L_\lambda}{E_\lambda} \tag{4}$$

Once we calculate SWIm image radiance values it is possible to estimate the Global Horizontal Irradiance (GHI) by integrating the image radiance values over the hemispherical sky dome. The GHI is a wide spectrum measurement typically made from about 300nm to 3000nm. SWIm considers a narrower range from 400nm to 800nm. Despite this inconsistency we can take advantage of the fact that when integrating over the wide spectrum, the resulting radiance is nearly proportional to the spectral radiance at 540nm. The proportionality holds for the solar spectrum, and typical modifications of this spectrum resulting from Rayleigh and Mie scattering. For example a normalized Rayleigh spectrum has more intensity in the blue wavelengths and less in the red and IR compared with the solar spectrum. The break even point is close to 540nm, and happens to be close to the 550nm standard often used to represent the peak sensitivity in human vision. This is borne out in preliminary case studies comparing SWIm generated GHI values to actual GHI values measured with a pyranometer at the National Renewable Energy Laboratory (NREL), in Golden, CO. We are presently working to refine this algorithm with a correction parameter based on atmospheric water

https://doi.org/10.5194/amt-2019-81
Preprint. Discussion started: 3 June 2019

Atmospheric Measurement Techniques Discussions

vapor content, since this does have a more selective effect in the near-IR wavelengths. Similar calculations can be made for direct and diffuse solar irradiance.

3.2 Moonlight, city lights, and other light sources

During the night the moon can replace the sun as an angularly localized light source (e.g., Miller et al., 2009). In the present study, the lunar radiance is calculated from considerations of its astronomical magnitude as a function of phase angle (180° - scattering angle). Near full moon a correction is added based on the opposition effect and potential lunar eclipses. At phase angles of less than ~4° the brightness is increased by up to ~20%, except the brightness is reduced substantially to factor in lunar eclipses as we move closer to 0° phase angle. Near new moon a term for Earthshine is taken into account, since this becomes significant compared with reflected sunlight from the lunar crescent. Earthshine is sunlight reflected first from the Earth's surface, then from the moon's surface.

Other light sources such as city lights, airglow, zodiacal light, individual stars and galactic glow are also included. An approximate scattering calculation is performed for city lights emanating from spatially extended areas with respect to the gas, aerosols, and cloud components of the atmosphere.

Since the Earth can be approximated as a spherical object, various twilight phenomena can be displayed via spherical geometry accommodated by SWIm. The varying path of light through the curved atmosphere enables the reproduction of observable optical effects, including changes in clear sky and cloud colors. Effects relating to the Earth's shadow (including blockage by the terrain and attenuation by the lower atmosphere) are also represented, affecting both the molecular atmosphere and cloud related radiative processes. The "Belt of Venus" can be simulated when a moderate amount of high-altitude aerosols scatter red light just above the Earth's shadow.

3.3 Clear sky ray-tracing

To cover the full extent of atmosphere beyond the NWP model domain, a "clear sky" ray-tracing (Step 2) is conducted though on a coarser angular grid compared with Step 1. The primary purpose of Step 2 is to provide a more direct account of the radiance produced by Rayleigh scattering. A second purpose is to model the effect of aerosols that may extend beyond the top of the model grid, specified via a 1-D stratospheric variable. Both stratospheric aerosols and twilight phenomena benefit from the vertical extent considered in this step, all the way up to about 100km.

https://doi.org/10.5194/amt-2019-81
Preprint. Discussion started: 3 June 2019

3.4 Hydrometeors

As the light rays are traced through the model grid (yellow rays in Fig 2.) their attenuation is determined by considering the optical thickness of intervening clouds and aerosols along their paths. A two-stream approach is used to incorporate the backscatter fraction to determine the total downward illumination (direct + forward scattered) at a particular model grid point. Considering the direct illumination component, the hydrometeor extinction coefficient is largely dependent on the effective radius of the cloud hydrometeor size distribution. The expression in eq. 5 is adapted from (Stephens, 1978).

$$\alpha = \frac{1.5\,CWC}{r_e \varrho_h} \tag{5}$$

Where α is the extinction coefficient, CWC is the condensed water content, r_e is the effective radius, and ϱ_h is the hydrometeor density -- all defined at the current model grid point.

The effective radius is specified based on hydrometeor type and (for cloud liquid and ice) CWC. For cloud liquid and cloud ice, larger values of CWC translate to having larger r_e and smaller α. In other words larger hydrometeors have a smaller area to volume ratio and scatter less light per unit mass. When we trace light rays through a particular grid box, the values of CWC are bilinearly interpolated to help prevent rectangular prism shaped artifacts from appearing in the images.

3.4.1 Single Scattering

The single scattering phase function has a sharp peak near the sun (i.e. forward scatter) that generally becomes stronger in magnitude for larger hydrometeors. Cloud ice and snow also have sharper forward peaks than liquid, particularly for pristine ice. A linear combination of Henyey-Greenstein functions (Henyey and Greenstein, 1941) is employed to specify the angularly dependent scattering behavior (phase function) for each hydrometeor type, producing curves shown in Figure 3. Given the values of asymmetry factor g, the individual Henyey-Greenstein terms (6) are formulated here to integrate to a value of 4π over the sphere, so that their average (normalized) value is 1, thus conserving energy.

https://doi.org/10.5194/amt-2019-81
Preprint. Discussion started: 3 June 2019

Atmospheric Measurement Techniques
Discussions

$$P_i(\theta) = \frac{1 - g_i^2}{[1 + g_i^2 - 2g_i \cos(\theta)]^{3/2}} \quad (6)$$

The overall phase function is given by

$$P(\theta) = \sum_i c_i P_i(\theta) \quad (7)$$

When $\tau << 1$ we can use a thin atmosphere approximation to estimate the solar relative spectral radiance due to single scattering.

$$L'_\lambda \simeq P(\theta)\,\tau \quad (8)$$

This relationship applies to hydrometeors as well as aerosols and the molecular atmosphere. In practice, the ray tracing algorithm considers extinction between the sun and the scattering surface as well as between the scattering surface and the observer.

3.4.2 Multiple scattering

When the optical thickness along the forward or backward paths approaches or exceeds unity, contributions to the observed signal from multiple scattering events become too significant to approximate via single-scatter. A rigorous, though time-consuming approach such as Monte-Carlo would consider each scattering event explicitly. Instead, here we use a more efficient approximation that arrives at a single scattering phase function that approximates the bulk effect of the multiple scattering events. Several terms that interpolate between optically thin and thick clouds are used as input for this parameterization as described below.

Thick clouds seen from near ground level can be either directly or indirectly illuminated by the light source. Inspection of the light rays in figure 2 helps show that direct illumination corresponds to $\lim_{\tau_o \to 0} \tau_s = 0$. A fully lit cloud surface will by definition have no intervening material between it and the sun. Conversely, indirect illumination implies that $\lim_{\tau_o \to 0} \tau_s >> 0$. The indirect illumination case is assumed to have anisotropic brightness dependent on the upward viewing zenith angle z of each image pixel. This modulates the transmitted irradiance value associated with the point where this light ray intersects the cloud. For an example with a heavy overcast sky, we use a normalized brightness given by $\frac{1+4\cos(z)}{3}$, providing a darker sky near the horizon and a steadily brightening sky toward the zenith. This generally matches observed camera images in cases with low surface albedo. A rationale for this is that when looking near

https://doi.org/10.5194/amt-2019-81
Preprint. Discussion started: 3 June 2019

the horizon, the multiple scattering events have a higher probability of having at least one surface reflection, resulting in an increased probability of photon absorption. The direct illumination case is similar except that the irradiance value is given by the solar irradiance and the relative brightness depends on the scattering angle, peaking in the antisolar direction.

Intermediate values of τ_o are given empirical phase functions with decreasing values of g as τ_o increases, similar to the concepts described in Piskozub and McKee, 2011. As τ_o increases with thicker clouds, the scattering order also increases and the effective phase function becomes flatter.

3.4.3 Cloud Layers Seen from Above

As a simple illustration for cases looking from above we consider a homogeneous cloud of hydrometeors having optical thickness τ, being illuminated with the sun at the zenith (i.e. $z_o = 0$). The cloud albedo (assuming a dark land surface) can be parameterized as:

$$a = \frac{b\tau}{(1+b\tau)} \tag{9}$$

where b is the backscatter fraction (Stephens, 1978). τ here is considered to be along the slant path of the light rays coming from the sun (τ_s in Fig. 2). For values of $\tau \leq 1$, we can assume single scattering and $a \sim b\tau$, while for large τ, $a > 0.9$ and asymptotes to just below 1.0 (not reaching 1.0 identically due to the presence of a very small absorption component term).

For $\tau >> 1$ (asymptotic limit) the cloud albedo a can be translated into an approximate reflectance value through a division by μ_o, where $\mu_o = cos\, z_o$. This is the case since thick cloud (or aerosol) layers act approximately as Lambertian reflectors (with $g \rightarrow 0$) for the high order scattering component (Piskozub and McKee, 2011, Gao et al., 2013, Bouthers et al., 2008). When a given photon is scattered many times, the stochastic nature of the scattering causes the correlation between the direction of propagation of the photon and the direction of incident radiation to greatly decrease. To improve the accuracy so we can address the anisotropies that do occur when looking at cloud layers from above. A simple bidirectional reflectance distribution function (BRDF) is thus being developed in the form of an anisotropic reflectance factor (ARF). When all orders of scattering are considered, the ARF remains relatively close to 1 when the solar zenith angle z_o is small. A large solar zenith angle will show preferential forward scattering causing the ARF to increase markedly with low scattering angles. Even with this

https://doi.org/10.5194/amt-2019-81
Preprint. Discussion started: 3 June 2019

enhancement, inspection of ABI satellite imagery suggests the reflectance factor, $\mu_o \times ARF$, generally stays below 1.0 in forward scattering cases.

In cases where $\tau < 1$ we are in a single scattering (or low-order) regime and the dependence of reflectance on μ_o goes away. In practice, this means that thicker aerosol (or cloud) layers will generally decrease in reflectance with a large z_o, while the reflectance holds more constant for very thin layers (assuming molecular scattering by the gas component is small). This causes the relative brightness of thin aerosol layers, compared with thicker clouds and the land surface to increase near the terminator. Interpolation is used to approximate the reflectance between the low τ and high τ regimes.

3.5 Aerosols

SWIm applications in a Multidisciplinary University Research Initiative (MURI) called "Holistic Analysis of Aerosols in Littoral Environments" (HAALE) required improvements to the treatment of atmospheric aerosol. There are two general methods for working with aerosols in SWIm. The first uses a 1-D specification of the aerosol field that runs somewhat faster. The second, newer, approach considers the 3-D aerosol distribution described in detail herein. Aerosols are specified by a chemistry model in the form of a 3-D extinction coefficient field. Various optical properties are assigned based on the predominant type (species) of aerosols present in the model domain.

3.5.1 Single Scattering

To determine the scattering phase function clouds and aerosols are considered together and aerosols are simply considered as another species of hydrometeors. For a case of aerosols only, the phase function $P(\theta)$ is defined depending on the type of aerosol. The Double Henyey-Greenstein (DHG) function (Louedec et al., 2012) is the basis of what is used to fit the phase function.

$$P(\theta, g, f_b) = (1 - g^2)\left[\frac{1}{1+g^2 - 2g\cos(\theta)} + f_b\left(\frac{3\cos^2(\theta) - 1}{2(1+g^2)^{3/2}}\right)\right] \quad (10)$$

This function has the property of integrating to 1 over the sphere representing all possible light ray directions - θ is the scattering angle, and the asymmetry factor g

https://doi.org/10.5194/amt-2019-81
Preprint. Discussion started: 3 June 2019

Atmospheric Measurement Techniques Discussions

represents the strength of the forward scattering lobe. The weaker lobe in the back scattering direction is controlled by f_b.

Dust generally has a bimodal size distribution of relatively large particles. For this a linear combination of a pair of DHGs can be set by substituting g_1 and g_2 for g. As an example we can assign $g_1 = .962$, $g_2 = .50$, $f_b = .55$, $f_c = .06$, where f_b is the term for the backscatter peak and f_c is the fraction of photons assigned to the DHG using g_1 :

$$P(\theta, g_1, g_2, f_b) = f_c P(\theta, g_1, f_b) + (1 - f_c) P(\theta, g_2, f_b) \quad (11)$$

Smoke and haze are composed of finer particles. Here we can also specify a combination of g_1 , g_2, and f_c to help in fitting the phase function. The asymmetry factor values of g, g_1 and g_2 each have a slight spectral variation to account for the variation in size parameter with wavelength. This means that a slight concentration of bluer light occurs closer to the sun or moon. The overall asymmetry factor g is related to the component factors g_1 and g_2 as follows:

$$g = f_c g_1 + (1 - f_c) g_2 \quad (12)$$

g_1 and g_2 are allowed to vary slightly between the three reference wavelengths (Section 3). In addition, each application of the DHG function uses an extinction coefficient that varies according to an Angstrom exponent, that in turn depends on the asymmetry factor g at 546nm. This allows for the spectral dependence of extinction. Coarser aerosols will have a higher asymmetry factor (i.e. a stronger forward scattering lobe), a lower Angstrom exponent and a more uniform extinction at various wavelengths giving a more neutral color. The value of f_c can be set to reflect contributions from a mixture of aerosol species. We can thus specify the phase function with four parameters g_1 , g_2, f_c, and f_b.

The single scattering albedo ω can also be specified for each wavelength to specify the fraction of attenuated light that gets scattered. ω represents the probability that a photon hitting an aerosol particle is scattered rather than absorbed, thus darker aerosols have ω significantly less than 1. The spectral dependence of ω is most readily apparent in the color of the aerosols as seen with back scattering. This applies either to a surface view opposite the sun, or to a view from above (e.g. space). Taking the example of hematite dust, the single scattering albedo ω is set to 0.935, 0.92, and

0.86 for our Red/Green/Blue reference wavelengths, respectively. This can eventually interface with a library of optical properties for a variety of aerosol types.

3.5.2 Aerosol Optical Properties Assignment

In its current configuration, aerosol optical properties for the entire domain are assumed to be characterized by a single set of parameters in SWIm, reflecting the behavior of a predominant type or mixture of aerosols. The first row in Table 2 was derived semi-empirically for relatively dusty days in Boulder, CO based on a comparison between simulated and camera images and visual observations. These days feature a relatively condensed aureole around the sun indicative of a contribution by large dust particles to a bimodal aerosol size distribution. This type of distribution has often been observed in AERONET retrievals. The single scattering albedo is set with increased blue absorption as might be expected for dust containing a hematite component.

The second case of mixed dust and pollution was derived from AERONET observations over Saudi Arabia, calculating the phase function using Mie scattering theory (Appendix A), then applying a curve fitting procedure to yield the four phase function parameters described previously. In this case the single scattering albedo is spectrally independent. Simulated images for these two sets of phase function parameters are shown in Fig. 4.

Case	g_1	g_2	f_c	f_b	ω
Colorado Dust	.59, .60, .61	.895, .900, .905	.12, .12, .12	.550, .550, .550	.935, .92, .86
Saudi Arabian Mixed Dust and Pollution	.23, .27, .29	.915, .925, .933	.58, .54, .53	.562, .558, .558	.96, .96, .96

Table 2. Two cases showing the four fitted phase function parameters g_1 , g_2, f_c, and f_b as well as single scattering albedo ω , for each of the three reference wavelengths, 615nm, 546nm and 450nm.

3.5.3 Aerosol Multiple Scattering

https://doi.org/10.5194/amt-2019-81
Preprint. Discussion started: 3 June 2019

Atmospheric Measurement Techniques
Discussions

As with meteorological clouds, when the aerosol optical thickness along the forward or backward ray paths (Fig 2) approaches or exceeds unity, the contributions from multiple scattering increase. As with cloud multiple scattering, a rigorous approach such as Monte-Carlo would consider each scattering event explicitly, though this would be computationally inefficient. Once again, we appeal to a more efficient approximation that determines a single scattering phase function that is equivalent to the net effect of the multiple scattering events.

3.5.4 Aerosol Layers Seen from Above

Non-absorbing aerosols seen from above can be treated in a similar manner to cloud layers as described above (eq. 6). We now extend this treatment to address absorbing aerosols. Along with 3-D aerosol fields from the CIRA chemistry (RAMS and WRF) model analyses and forecasts, SWIm was tested with two other chemistry models, HRRR-Smoke (Fig 6, available at https://rapidrefresh.noaa.gov/hrrr/HRRRsmoke) and the Navy Global Environmental Model (NAVGEM - Fig 5). This yielded valuable information about how multiple scattering in absorbing aerosol layers can be handled.

For partially absorbing aerosols such as smoke containing black carbon or dust, in a thin layer we can multiply eq. (6) by ω, the single scattering albedo to get the aerosol layer albedo.

$$a = \omega \frac{b\tau}{(1+b\tau)} \tag{13}$$

A more challenging case to parameterize is when $\tau \gg 1$ and multiple scattering is occurring. Each extinction event where a photon encounters an aerosol particle now also has a non-zero probability of absorption occurring. Here we can consider a probability distribution for the number of scattering events for each photon that would have been received by the observer if the aerosols were non-absorbing (e.g. sea salt where $\omega \sim 1$). We can define a new quantity ω' to represent a multiple scattering albedo.

$$a = \omega' \frac{b\tau}{(1+b\tau)} \tag{14}$$

For typical smoke or dust conditions a will approach an asymptotic value between about 0.3 to 0.5. We plan to check the consistency of SWIm assumptions with previous work in this area such as in (Bartkey, 1968). Once the albedo is determined a phase

https://doi.org/10.5194/amt-2019-81
Preprint. Discussion started: 3 June 2019

function is used for thin aerosol scattering and a BRDF is used for thick aerosols. This is similar to the way that clouds are handled.

3.6 Combined clear sky and aerosol/cloud radiances

The clear sky radiance is calculated through the whole atmosphere, while the aerosol and cloud radiances are determined within the more restricted volume of the model grid. As a post-processing step these quantities are merged together to provide the combined radiance at each location in the scene from the observer's vantage point.

3.7 Land Surface

When a backward-traced ray starting at the observer intersects the land surface we consider the incident and reflected light upon the surface that contributes to the observed light intensity, as attenuated by the intervening gas, aerosol, and cloud elements. The land spectral albedo is obtained at 500m resolution using the Blue Marble Next Generation Imagery (BMNG, Stockli et al., 2005). The BMNG image RGB values are functionally related to spectral albedo for three Moderate Resolution Imaging Spectroradiometer (MODIS) visible wavelength channels. A spectral interpolation is performed to translate the BMNG / MODIS albedos into the three reference wavelengths used in SWIm.

For higher resolution display over the continental United States, an aerial photography dataset obtained from the United States Department of Agriculture (USDA) can also be used (Figs 3.6, 3.7). The associated National Agriculture Imagery Program (NAIP) data are available at 70cm resolution and is added to the visualization at sub-grid scales with respect to the model Cartesian grid. This dataset is only roughly controlled for spectral albedo, though it can be a good tradeoff with its very high spatial resolution.

To obtain the reflected surface radiance in each of the three reference wavelengths, we utilize clear-sky estimates of direct and diffuse incident solar irradiance. For the direct irradiance component, spectral albedo is converted to reflectance using the anisotropic reflectance factor f that depends on the viewing geometry and land surface type. Thus the reflectance $\varrho = af$ where a is the terrain albedo. We calculate the solar relative spectral radiance of the land surface as

$$L'_{\lambda} = \frac{4\,\varrho\,E_{\lambda H}}{E_{\lambda}} \tag{15}$$

https://doi.org/10.5194/amt-2019-81
Preprint. Discussion started: 3 June 2019

where $E_{\lambda H}$ is the global horizontal spectral irradiance. This relationship can also be used for the diffuse irradiance component if we assign $f = 1$. Relatively simple analytical functions for f are used over land. Modified values of surface albedo and f are used in the presence of snow or ice cover. A sun glint model with a fixed value of mean wave slope is used over water. Scattering from below the water surface is also considered. In the future, wave slope will be derived from NWP ocean wave and wind forecasts.

Terrain elevation data on the NWP model grid is used to help determine where light rays may intersect the terrain.

3.8 Translation into displayable color image

As explained earlier, spectral radiances are computed within the software for three narrowband wavelengths, using solar-relative intensity units to yield a scaled spectral reflectance. This allows some flexibility for outputting spectral radiances, spectral reflectance, or more visually realistic imagery that accounts for details in human color vision and computer monitor characteristics. To accomplish the latter it is necessary to estimate spectral radiance over the full visible spectrum using the partial information from the selected narrowband wavelengths we have so far. The procedure is to first perform a polynomial interpolation of the three narrowband (solar relative) reflectance values, then multiply this by the solar spectrum, helping to fill the gaps and yield full spectral radiance information at each pixel location. The observed solar spectrum interpolated in 20nm steps is used for purposes of subsequent numerical integration. Having a full spectrum is important when computing an accurate human color vision response [Bell et al., 2006].

Digital RGB color images are created by calculating the image count values with three additional steps:

1) Convolve the spectral radiance (produced by the step described in the above paragraph) with the CIE tristimulus color matching response functions to account for color perception under assumptions of normal human photopic vision. Each pixel of the image now specifies the perceived color in the XYZ color space (Smith and Gould, 1931). In this color system the chromaticity (related to color hue and saturation) is represented by normalized xy values and the perceived brightness is the Y value. The normalization of the XYZ values to yield chromaticity specifies that x+y+z=1. The xyz chromaticity values represent the normalized perception for each of the three primary colors. An example illustrating the benefits of this procedure is the blue appearance of the daytime sky. The violet component of the light is actually stronger than blue, but has

https://doi.org/10.5194/amt-2019-81
Preprint. Discussion started: 3 June 2019

less impact on the perceived color since we are less sensitive to light at that wavelength.

2) Apply the 3x3 transfer matrix that puts the XYZ image into the RGB color space of the display monitor. This is needed in part because the colors of the display system are not spectrally pure. Another consideration is the example of spectrally pure violet light, perceived in a manner similar to purple (a mix of blue and red for those with typical trichromatic color vision). Violet is beyond the wavelengths that the blue phosphors in a monitor can show, so a small component of red light is mixed in to yield the same perception, analogous to what our eye-brain combination will do. We make the assumption that the sun (the main source of illumination) is a pure white color as is very nearly the case when seen from space thus setting the white point to 5800K, the sun's approximate color temperature. Correspondingly we also recommend setting one's display (e.g. computer monitor) color temperature to 5800K.

3) Include a gamma (approximate power law) correction with a value of 2.2 to match the non-linear monitor brightness scaling. This is important if we want the displayed image brightness to be directly proportional to the actual brightness of the scene, giving realistic contrast and avoiding unrealistically saturated colors.

This procedure is anticipated to give a realistic color and contrast match if one looks at a laptop computer monitor held next to the scene (with either ground- or space-based viewing). The results have somewhat more subtle colors and contrast compared with many Earth and sky images that we see. The intent here is to make the brightness of the displayed image proportional to the actual scene and perceived color to be the same as a human observer would see in a natural setting. This is without any exaggeration of color saturation prevalent in satellite "natural color" image rendering (e.g. Miller et al., 2012) and even in everyday photography. A more complete consideration of the effects of atmospheric scattering and absorption in image rendering softens the appearance of the underlying landscape when viewed from space or otherwise afar.

4. Applications

4.1 Demonstration of SWIm - Model Visualization

As we've seen, a fast 3-D radiative transfer package called Simulated Weather Imagery (SWIm) has been developed to serve in several roles relating to high-resolution model development and implementation. For example, visually and physically realistic images

https://doi.org/10.5194/amt-2019-81
Preprint. Discussion started: 3 June 2019

in full natural color (e.g., Miller et al., 2012) help to display output from model analyses and forecasts. At a glance one can see the fields of clouds, precipitation, aerosols and land surface in a realistic and intuitive manner. Model results are thus more effectively communicated for interpretation, displaying weather phenomena that can be seen in the sky and surrounding environment. SWIm readily conveys NWP information about current and forecast weather in an easily perceivable visual form to both scientific and lay audiences.

The SWIm package has been run an a variety of NWP modeling systems including the LAPS-Weather Research and Forecasting (WRF) system, Colorado State University (CSU) Regional Atmospheric Modeling System (RAMS) model, HRRR, and NAVGEM. We can thus discern general characteristics of the models including their handling of clouds, aerosols, and land surface (e.g. snow cover).

4.1.1 CSU RAMS Middle East Dust Case

Visualization of the RAMS model developed at Colorado State University was done for a case featuring dust storms over the Arabian Peninsula and the neighboring region (Miller et al., 2019; Bukowski et al., 2019), as part of the Holistic Analysis of Aerosols in Littoral Environments Multidisciplinary University Research Initiative (HAALE-MURI) project. Figure 9 shows the result of this simulation from in-situ vantage points just offshore from Qatar in the Persian Gulf at altitudes of 4km and 20m above sea level. With the higher vantage point we are above most of the atmospheric dust present in this case, so the sky looks bluer with Rayleigh scattering being more dominant instead of Mie scattering.

4.1.2 Additional Modeling Systems

Figure 6 shows a space-based perspective of December 2017 wildfires in Southern California using NWP data from the HRRR-Smoke system. Smoke plumes from fires and areas of inland snow cover are readily visible. Figure 7 depicts a simulated panoramic view from the perspective of an airplane cockpit at 1km altitude using LAPS analysis with 500m horizontal resolution. This is part of an animation designed to show how SWIm can be used in a flight simulator for aviation purposes. The visualization is using sub-grid scale terrain albedo derived from USDA 70cm resolution airborne photography acquired at a different time. SWIm has also been used to display LAPS-initialized WRF forecasts of severe convection (Jiang et al., 2015) showing a case with a tornadic supercell that produced a strong tornado striking Moore, Oklahoma in 2013.

https://doi.org/10.5194/amt-2019-81
Preprint. Discussion started: 3 June 2019

4.2 Validation of NWP analyses and forecasts

Simulated images and animations can be used by data assimilation and model developers as a validation to assess model performance and help guide improvements in initial and forecast fields, respectively. The imagery provides a qualitative validation of both the model fields and the visualization package when simulated images are compared against actual camera images. If in various situations simulated imagery can well reproduce observed images, this is an indication of the realism of the radiative transfer / visualization package (i.e., SWIm). Discrepancies between simulated and observed images in other cases may be interpreted as shortcomings in the analyzed or model forecast states.

The vantage point for such assessments can be on the ground, in the air, or from space (i.e. with multi-spectral visible satellite data). At a glance various obstructions to visibility can be intuitively seen in the imagery such as clouds, haze, and smoke. The land surface state including snow cover, visibility and illumination can be assessed. Figure 11 shows a cloud-free sky comparison where aerosol loading was relatively high due to smoke.

Solar irradiance computed by a solid angle integration of SWIm imagery can be compared with corresponding pyranometer measurements. For space-based satellite imagery, color images can be compared qualitatively and visible band reflectance can be used for quantitative comparison.

SWIm has been tested with a variety of models. An example is an NWP system that produces very rapid update (5-15min) and very high resolution (e.g. 500m) analyses and forecasts (Local Analysis and Prediction System - LAPS, Toth et al., 2014). The cloud analysis (Albers et al., 1996, Jiang et al., 2015) of LAPS uses satellite (including IR and 1-km resolution visible imagery, updated every 15-min), METAR, radar, and aircraft observations along with a first guess forecast to produce 3-D fields of cloud and hydrometeor variables. The LAPS cloud analysis is running regionally at 500m horizontal resolution on a 5- to 10-min update cycle. The 3-D hydrometeor fields are analyzed using satellite, radar, surface ceilometer observations, and model first guess fields. The largely sequential data insertion procedure of today's LAPS is being updated with a 3/4DVAR cloud analysis module that in the future will be used both in LAPS and other fine scale data assimilation systems.

https://doi.org/10.5194/amt-2019-81
Preprint. Discussion started: 3 June 2019

Atmospheric Measurement Techniques Discussions

Comparing analyses from LAPS with day-time and night-time camera images under cloudy, precipitating, and clear/polluted air conditions, SWIm was tested and can realistically reproduce rainbows, twilight sky colors and other atmospheric phenomena (Albers and Toth, 2018). Since camera images are not yet used as observational input in LAPS, subjective and quantitative comparisons of high resolution observed and simulated weather imagery provides a valuable opportunity to assess the quality of cloud analyses and forecasts from various NWP systems, including LAPS, Gridded Statistical Interpolation (GSI), High Resolution Rapid Refresh (HRRR), Finite Flow Following Icosahedral Model (FIM), and the NAVGEM.

360° imagery, presented in either a polar or cylindrical projection, can show either analysis or forecast fields. Here, we present the results of ongoing developments of this simulated imagery, along with comparisons to actual camera images produced by a network of all-sky cameras that is located within our Colorado 500m resolution domain, as well as space-based imagery. These comparisons check the skill of the existing analysis of clouds and other fields (e.g. precipitation, aerosols, and land surface) at high-resolution.

4.2.1 Ground-based observations

Figure 10 shows a comparison between a simulated all-sky image and an observed camera view at the same time. The simulated image was derived from a LAPS cloud analysis running at 500m horizontal resolution on a 5-min update cycle. The camera image provides an independent validation of the analysis. In this case we see locations of features within a thin high cloud deck are reasonably well placed. Variations in simulated and observed cloud opacity (and optical thickness) are also reasonably well matched. This is evidenced by the intensity of the light scattering through the clouds relative to the surrounding blue sky, as well as the size (and shape) of the brighter aureole closely surrounding the sun. The brightness scaling being used for both images influences the apparent size of the the inner bright (saturated) part of the solar aureole in the imagery. The size also varies with cloud optical thickness and reaches a maximum angular radius at $\tau \sim 3$.

It is also possible to compare simulated and camera images to validate gridded fields of model aerosol variables. In figure 11 we see such a comparison using a simple 1-D aerosol analysis for a smoky day in Boulder, Colorado when the AOD was measured by a nearby Aeronet station to be 0.7.

4.2.2 Space-based observations

https://doi.org/10.5194/amt-2019-81
Preprint. Discussion started: 3 June 2019

Atmospheric Measurement Techniques Discussions

Figure 12 shows observed imagery from the Earth Polychromatic Imaging Camera (EPIC) imagery aboard the Deep Space Climate Observatory (DSCOVR) satellite, used as independent validation in a comparison with a simulated image from Global LAPS (G-LAPS) fields visualized using SWIm. The analysis shown here comprises 3-D cloud liquid and cloud ice fields hourly at 21km resolution, in addition to other state and surface variables. Visible and IR satellite imagery are utilized from GOES-16 and GOES-17, with first guess fields from a GFS forecast.

The horizontal location and relative brightness of the simulated vs. observed clouds match fairly closely in the comparison for many different cloud systems over the western hemisphere. The land surface spectral albedo also appears to be in good agreement, including areas of snow north of the Great Lakes. The sun glint model in SWIm shows the enhanced brightness surrounding the nominal specular reflection point in the ocean areas surrounding the Yucatan peninsula due to sunlight reflecting from waves assumed to have a normal slope distribution. This can help with evaluation of a coupled wind and ocean wave model. There is some difference in feature contrast due to a combination of cloud hydrometeor analysis and SWIm reflectance calculation errors, as well as uncertainty in the brightness scaling of the DSCOVR imagery, along with uncertainties in the snow albedo over vegetated terrain. The DSCOVR imagery was empirically reduced in contrast to represent the same linear brightness (image gamma - Sec. 3.8) relationships used in SWIm processing.

Figure 13 shows a comparison of the RAMS model run discussed earlier with a corresponding color image generated from MODIS Aqua data. Features representing lofted dust are depicted over the Arabian peninsula and over the Persian Gulf. Liquid (low) and ice (high) clouds can be seen. The microphysics and chemistry formulations in the RAMS model can be assessed and improved based on this comparison, such as minimizing an excess of cloud-ice in the model simulation. The amount of dust east of Qatar over the water appears to be underrepresented in this model run.

4.2.3 Objective measures

In advanced validation and data assimilation (Section 4.3) applications an objective measure is desired for the comparison of observed and simulated imagery. For simple measures of similarity, cloud masks can be derived from both a SWIm and a corresponding camera image, using for example sky color (e.g. red/blue intensity ratios). Categorical skill scores can then be used to assess the similarity of the angular or horizontal location of the clouds.

https://doi.org/10.5194/amt-2019-81
Preprint. Discussion started: 3 June 2019

Atmospheric Measurement Techniques Discussions

To assess the spatial coherence of image values (thus radiances) between the simulated and observed images, the Pearson correlation coefficient r can be used. The mean value of r, calculated for the set of simulated vs. observed pixel intensities in each of the image channels R, G, B, is denoted as $\bar{r}$. We consider this to be a measure of overall image similarity. The R channel is generally most sensitive to clouds and large aerosols, with blue emphasizing Rayleigh scattering contributions from air molecules and Mie scattering from small aerosols. The G channel is sensitive to land surface vegetation and sky colors that can occur around sunset and twilight. Over many cases of SWIm vs. camera image comparisons, $\bar{r}$ was found to correspond well to the subjective assessment of the sky spectral radiance patterns, circumventing biases arising due to a lack of radiance calibration in many types of cameras.

$\bar{r}$ values reveal how realistic the optical and microphysical properties of the analyzed clouds and aerosols are, in addition to feature locations. When $\bar{r}$ < 1, this reflects possible deficiencies in the quality of (i) the 3D digital analysis or specification of hydrometeors, aerosols, and other variables; (ii) the calibration of observed camera images, and (iii) the realism or fidelity of the SWIm algorithms. Recognizing that (a) with all their details, visible imagery is high dimensional and good matches are extremely unlikely to occur by chance, and that (b) high $\bar{r}$ values attest to good performance in all three aspects listed above (i, ii, and iii), the occurrence of just a few cases with high $\bar{r}$, as long as they span various atmospheric, lighting, and observing position conditions, may be sufficient to demonstrate the realism of the SWIm algorithms. For example, the correlation coefficient between the two images in figure 11 is 0.961, indicating the smoke induced aureole around the sun (caused by forward scattering) is well depicted by SWIm.

4.3 Assimilation of camera and satellite imagery

With new geostationary satellite instruments such as ABI now available, we have an abundance of high-resolution satellite data in the spatial, temporal, and spectral domains. As ground-based camera networks also become more readily available we envision a unified assimilation of camera, satellite, and other data sets in NWP models. SWIm can be used with camera images (and possibly visible satellite images) as a forward operator to constrain model fields in a variational minimization. One approach would entail developing SWIM's Jacobian or adjoint, while other techniques employ recursive minimization. Observed camera images can thus be assimilated within a 3/4DVAR cloud analysis module. 3D- and 4DVAR has been proposed to utilize infrared and visible satellite data (Vukicevic et al., 2004, Polkinghorne and Vukicevic, 2011).

https://doi.org/10.5194/amt-2019-81
Preprint. Discussion started: 3 June 2019

Atmospheric Measurement Techniques Discussions

Such capabilities may be useful in NWP systems such as GSI, Joint Environment for Data Integration (JEDI), variational LAPS (vLAPS), and various global models. Thus SWIm can be combined with other forward operators (such as the CRTM and SHDOM) for comparison with camera and satellite data. Along with additional observational data (e.g. RADAR, METARs), and model physical, statistical, and dynamical constraints we can provide a more complete 3-D and 4-D variational assimilation to drive a very fine scale cloud-resolving model. This moves toward the goal of having the model be more consistent with full resolution radar and satellite data.

We are experimenting with methodologies to use camera images for calculating a penalty term in a variational cost function. A promising approach is to utilize the $\bar{r}$ metric described above. Two non-variational assimilation methods that are preliminary alternatives to using the Jacobian or adjoint have so far been tested with SWIm. One test (a single case run at this point) involves determining a translation vector applied to the entire 3D satellite-constrained cloud field to best fit the camera simulated image, maximizing $\bar{r}$. The second test involves constructing cloud clearing and adding masks based on color ratios seen in the simulated and/or actual camera images. A single iteration of an algorithm to modify the 3D cloud fields with the mask information often yields improvement in $\bar{r}$ judging from a series of real-time case studies.

To move towards the goal of comparing absolute radiance values two strategies are being considered. The first strategy would entail more precise calibration of camera exposure and contrast so images can be directly compared using a root mean square statistic. A second strategy entails using the simulated image to estimate Global Horizontal Irradiance (GHI) and then comparing with a GHI measurement made with a pyranometer colocated with the camera. The GHI estimation examines a calculated field of spectral radiance at 550nm, then extrapolates this to the wavelength integrated radiance at each angular location. Correction factors based on atmospheric pressure and water vapor can be added. As earlier noted, colors in the sky such as Rayleigh scattering happen to have crossover points in their normalized spectra with the solar spectrum that is close to the 550nm reference wavelength. This can be exploited when the radiance values are integrated over the hemisphere, normalizing by $cos(z)$ to yield the irradiance.

Since SWIm operates in three dimensions and considers multiple scattering of visible light photons within clouds it can help perform what is described as a tomographic cloud analysis. An example of tomographic analysis highlighting precipitating hydrometeors was performed with airborne passive microwave observations (Zhou et al., 2014).

Further examples include solving for a 3D cloud mask using a ground-based camera network as discussed in (Viekherman et al., 2014). This has been expanded using airborne camera image radiances to perform a 3D cloud liquid analysis (Levis, Schechner, Aides, 2015; Levis, Schechner et al., 2015) using a similar forward operator (SHDOM) in a variational solver using a recursive minimization. A corresponding aerosol Observation Simulation Experiment OSE analysis (Aides et al., 2013) was also performed with a ground-based camera network. A design for tomographic camera-based cloud analysis has more recently been developed (Mejia et. al., 2018).

5. Conclusions and Discussion

A visualization package that performs a fast 3-D radiative transfer in visible wavelengths called Simulated Weather Imagery (SWIm) has been presented. As summarized in Fig. 1, SWIm produces radiances in a wide variety of situations, even though other packages are more rigorous for particular situations they are designed for, at an increased computational cost. SWIm can be used to simulate color imagery of weather, including land surface conditions based on NWP analysis or forecast data in a visually realistic manner. SWIm images thus can be used to make complex and abstract NWP forecasts perceptually accessible, to subjectively and objectively assess the quality of NWP products, as well as to assimilate observed imagery via a comparison of such with simulated imagery produced by SWIm from first guess NWP forecasts.

An example of how SWIm can help forecasters with model interpretation and communication of weather information to the public is the possible dissemination of time-lapse sky camera views for both recent and future weather (near real-time and archived examples available at http://stevealbers.net/allsky/allsky.html). Interactive 3D flythroughs viewing from both inside and above the model domain can be an exciting way to display NWP model results for both scientific and lay audiences. This includes the use of in flight simulators for aviation purposes, along with other interactive game engines.

Beyond the use of existing camera networks, the installation and use of >180° field of view all-sky cameras at official meteorological observation sites could also be considered. High quality animations constructed with images from such cameras could be used to evaluate clouds, aerosols, and land surface features such as snow cover analyzed and forecast by NWP systems.

The full use of camera images will include their variational assimilation into high-resolution analysis states for the initialization of NWP forecasts used in

https://doi.org/10.5194/amt-2019-81
Preprint. Discussion started: 3 June 2019

Atmospheric Measurement Techniques Discussions

Warn-On-Forecasting (Stensrud et al., 2013). This can be especially useful in pre-convective environments where cumulus clouds are present while radar echoes have yet to develop. Today's DA techniques suffer in such situations, severely limiting the predictability of tornadoes and other high impact events. 4-D variational tomographic DA is designed to combine camera and satellite imagery from multiple viewpoints. The sensitive dependence of multiple scattering in 3D visible wavelength light propagation on the type and distribution of hydrometeors facilitates a better initialization of cloud properties throughout the depth of the clouds. This in turn can potentially extend the time span of predictability for severe weather events from the current period starting with the emergence of organized radar echoes back to the more subtle beginnings of cloud formation.

Methods and results related to the use of various light sources and the simulation of various twilight phenomena will be covered in separate publications. Current development of SWIm is focused on aerosol optical properties and multiple scattering. Ongoing work includes refinements to the single scattering albedo and the phase function for various types of aerosols, including dust and smoke. The parameterization being used to determine ω' is being revised to improve reflectance values associated with thick dust and smoke seen from space-based vantage points. Concurrently the improved parameterization of absorption with multiple-scattering will determine how dark it becomes for ground-based observers when heavy smoke and/or thick dust is present. Spectral variations in ω' become amplified as τ increases, causing the sky to have more saturated colors as it darkens.

As the spatiotemporal and spectral resolution of color imagery observed both with ground-based cameras and satellite-borne instruments and corresponding output from NWP models reaches unprecedented highs, a question arises whether variational DA methods can sensibly combine information from the two sources? Consistent analyses of clouds and related precipitation and aerosol fields would aid situational awareness and fine-scale model initialization. SWIm used as a 3-D forward operator for camera and visible satellite imagery may help addressing the above and related questions.

Acknowledgements:

This work was largely funded within the HALLE-MURI project supported by the Office of Naval Research (ONR). We thank Didier Tanre and the AERONET team for establishing and maintaining Capo Verde AERONET site used in this investigation. We also thank Afshin Andreas and Mark Kutchenreider of the National Renewable Energy Laboratory

(NREL) in Golden Colorado, along with Will Beuttell of EKO Instruments Inc. for help in accessing their real-time all-sky camera images.

References:

Aides A., Schechner Y. et al., Multi sky-view 3D aerosol distribution recovery. Optics express 21 (22): 25820-33, doi: https://doi.org/10.1364/oe.21.025820, 2013.

Albers S., and Toth, Z., Visualization, Evaluation, and Improvement of NWP-Based Cloud Analyses and Forecasts, JCSDA Newsletter Quarterly, 61, 17-26, doi: 10.25923/jw00-r987, 2018.

Albers S. et al.: The Local Analysis and Prediction System (LAPS): Analyses of Clouds, Precipitation, and Temperature, Weather and Forecasting, 11, 273-287, 1996.

Bannister R., Elementary 4D-VAR, DARC Technical Report No. 2. Data Assimilation Research Centre, University of Reading, UK, 2007.

Bartkey, The Reflectance of Homogeneous, Plane-parallel Clouds of Dust and Smoke, J. Quant. Spectrosc. Radiat. Transfer. 8, 51-68, 1968.

Bell, J. F. III, D. Savransky D., and Wolff M.J., Chromaticity of the Martian sky as observed by the Mars Exploration Rover Pancam instruments, J. Geophys. Res., 111, E12S05, doi:10.1029/2006JE002687, 2006.

Bodhaine, B A et al.: On Rayleigh Optical Depth Calculations. JTech 16, 11, 1854-1861, 1999.

Bouthers et al.: Interactive multiple anisotropic scattering in clouds, Proceedings of the 2008 symposium on interactive 3D graphics and games, 173-182, doi: 10.1145/1342250.1342277, 2008.

Bukowski, J. and van den Heever, S. C.: Effect of horizontal model resolution on the convective redistribution of mineral dust over the Arabian Peninsula. Submitted to Appl. Chem. Phys., 2019.

Doicu, A., Efremenko D., and Trautmann, T.: A multi-dimensional vector spherical harmonics discrete ordinate method for atmospheric radiative transfer. J. Quant. Spectrosc. Radiat. Transfer, 118, 121-131, doi: https://doi.org/10.1016/j.jqsrt.2012.12.009 , 2013.

Dubovik, O., Sinyuk, A., Lapyonok, T., Holben, B. N., Mishchenko, M., Yang, P., Eck, T. F., Volten, H., Muñoz, O., Veihelmann, B., van der Zande, W. J., Leon, J.-F., Sorokin, M., and Slutsker, I.: Application of spheriod models to account for aerosol particle nonsphericity in remote sensing of desert dust, J. Geophys. Res., 111, D11208, doi:10.1029/2005JD006619, 2006.

Evans, K. F.: The spherical harmonic discrete ordinate method for three-dimensional atmospheric radiative transfer. J. Atmos. Sci., 55, 429-446, 1998.

Henyey L.G. and Greenstein J.L.: Diffuse radiation in the galaxy, Astrophysical Journal 93:70-83, 1941

Gao M., Huang X., Yang P., and Kattawar G.W.: Angular distribution of diffuse reflectance from incoherent multiple scattering in turbid media, Appl. Opt. 52, 5869-5879, doi: https://doi.org/10.1364/AO.52.005869, 2013

Giles, D.M., Holben, B. N., Eck, T. F., Sinyuk A., Smirnov, A., Slusker I., Dickerson, R. R., Thompson, A. M., and Schafer, J. S.: An analysis of AERONET aerosol absorption properties and classifications representative of aerosol source regions, J. Geophys. Res., 117, D17203, doi:10.1029/2012JD018127, 2012.

Holben, B.N., Eck,T.F., Slutsker, I., Tanre, D., Buis, J. P., Setzer, A., E.Vermote, E, Reagan, J.A., Kaufman, Y.,.Nakajima, T., Lavenu, F., Jankowiak, I., and A.Smirnov, A.: AERONET - A federated instrument network and data archive for aerosol characterization, Rem. Sens. Environ., 66, 1-16, 1998

Jiang H. et al.: Real-Time Applications of the Variational Version of the Local Analysis and Prediction System (vLAPS). Bulletin of the American Meteorological Society 96 (12), 2045-2057, doi: https://doi.org/10.1175/bams-d-13-00185.1, 2015.

Kalnay E.: Atmospheric modeling, data assimilation and predictability. Cambridge university press, 341 pp., 2003.

Kleespies, T.J., van Delst P., McMillin L.M., and Derber, J., Atmospheric transmittance of an absorbing gas. 6. An OPTRAN status report and introduction to the NESDIS/NCEP Community Radiative Transfer Model, Appl. Opt., 43, 3103 – 3109, doi:10.1364/AO.43.003103, 2004.

Levis A., Y. Schechner, and Aides, A.:. Airborne Three-Dimensional Cloud Tomography. 2015 IEEE International Conference on Computer Vision (ICCV) (2015): 3379-3387, doi: https://doi.org/10.1109/iccv.2015.386, 2015.

Levis A., Schechner Y., et al.: An Efficient Approach for Optical Radiative Transfer Tomography using the Spherical Harmonics Discrete Ordinates Method, arXiv:1501.06093, 2015.

Louedec, K., Pierre Auger Collaboration & Losno, R. Atmospheric aerosols at the Pierre Auger Observatory and environmental implications, Eur. Phys. J. Plus, 127: 97, 2012.

Mayer B.: Radiative transfer in the cloudy atmosphere. European Physical Journal Conferences., 1:75-99, 2009.

Mejia, F. A., Kurtz, B., Levis, A., de la Parra, I., and Kleissl, J.: Cloud tomography applied to sky images: A virtual testbed. Solar Energy. 176. 287-300, doi: 10.1016/j.solener.2018.10.023., 2018.

Miller, S. D., Grasso, L., Bian, Q., Kreidenweis, S., Dostalek, J., Solbrig, J., Bukowski, J., van den Heever, S. C., Wang, Y., Xu, X., Wang, J. Walker, A., Zupanski, M., Wu, T.-C., Chiu, C., and Reid, J.: A Tale of Two Dust Storms: Analysis of a Complex Dust Event in the Middle East, Submitted to Atmos. Meas. Tech., 2019.

Miller, S. D., C. C. Schmidt, T. J. Schmit, and D. W. Hillger: A case for natural colour imagery from geostationary satellites, and an approximation for the GOES-R ABI, Int. J. Rem. Sens., 33(13), 3999-4028, 2012.

Miller, S.D., and Turner R.E.: A Dynamic Lunar Spectral Irradiance Data Set for NPOESS/VIIRS Day/Night Band Nighttime Environmental Applications, IEEE Trans. Geosci. Remote Sens., 47(7), 2316-2329, doi:10.1109/TGRS.2009.2012696, 2009.

Piskozub, J. and McKee, D.: Effective scattering phase functions for the multiple scattering regime. Optics express. 19. 4786-94, doi:10.1364/OE.19.004786, 2011.

Polkinghorne R., and Vukicevic T.: Data Assimilation of Cloud-Affected Radiances in a Cloud-Resolving Model. Monthly Weather Review. 139. 755-773, doi: 10.1175/2010MWR3360.1, 2011.

Schmit, T. L., Griffith P., Gunshor M.M., Daniels J.M., Goodman S.J., and Lebair W.J.: A closer look at the ABI on the GOES-R series. Bull. Amer. Meteor. Soc., 98, 681-698, doi: https://doi.org/10.1175/bams-d-15-00230.1, 2017.

Smith T., and Guild J.: The C.I.E. colorimetric standards and their use. Trans. Opt. Soc. 33 73, 1931.

Stensrud D. et al.: Progress and challenges with Warn-on-Forecast. Atmospheric Research. 123. 2-16. 10.1016/j. Atmosres.2012.04.004, 2013.

Stephens G.L.: Radiation Profiles in Extended Water Clouds. II: Parameterization Schemes Journal of the Atmospheric Sciences November 1978, 35, (11), 1978.

Stockli R. et al.: The Blue Marble Next Generation—A true color Earth dataset including seasonal dynamics from MODIS, Nasa Earth Observatory, 2005.

Toth, Z., Albers S., and Xie Y.: Multiscale Data Assimilation and Forecasting. Bull. Amer. Meteor. Soc.,95 (2). ES30-ES33, doi: https://doi.org/10.1175/bams-d-13-00088.1, 2014.

Toth, Z., Buizza R.: Weather Forecasting: What Sets the Forecast Skill Horizon? In: The Gap Between Weather and Climate Forecasting: Subseasonal to Seasonal Prediction, 17-45. Eds.: A. Robinson and F. Vitard. Elsevier, 978-0-12-811714-9, doi: https://doi.org/10.1016/b978-0-12-811714-9.00002-4, 2019.

Veikherman D., Aides A., Schechner Y.Y., and Levis, A.: Clouds in The Cloud. Proc. ACCV, 659-674, doi: https://doi.org/10.1007/978-3-319-16817-3_43, 2014.

https://doi.org/10.5194/amt-2019-81
Preprint. Discussion started: 3 June 2019

Atmospheric Measurement Techniques
Discussions
Open Access
EGU

Vukicevic T. et al.: Mesoscale Cloud State Estimation from Visible and Infrared Satellite Radiances. Monthly Weather Review. 132. 10.1175/MWR2837.1, 2004.

Zhou J. et al.: A Fast Inverse Algorithm Based on the Multigrid Technique for Cloud Tomography. Journal of Atmospheric and Oceanic Technology. 31. 1653-1662, doi: 10.1175/JTECH-D-13-00184.1, 2014.

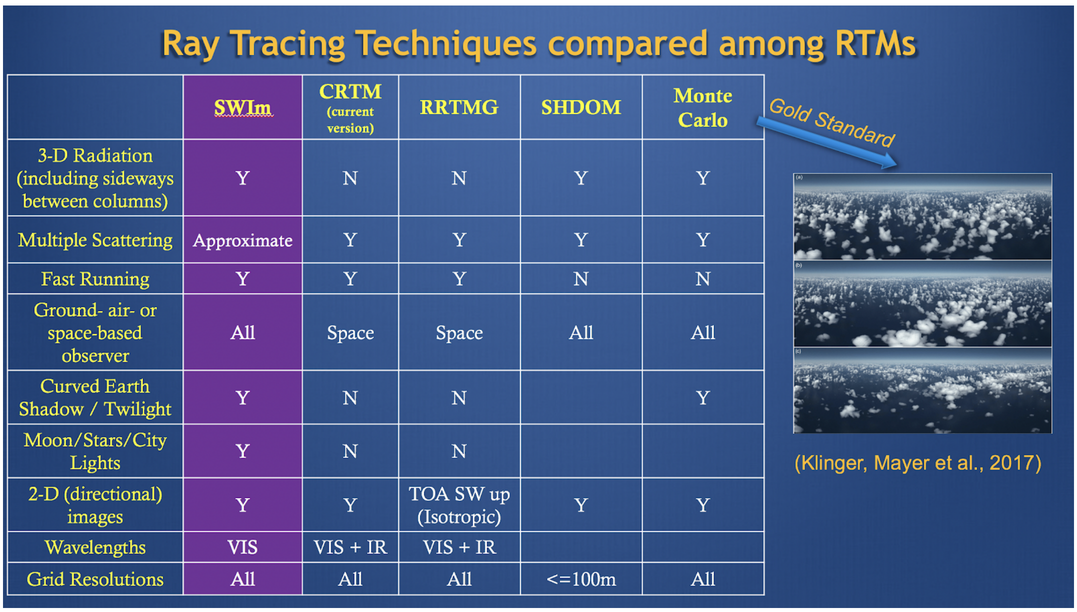

	SWIm	CRTM (current version)	RRTMG	SHDOM	Monte Carlo
3-D Radiation (including sideways between columns)	Y	N	N	Y	Y
Multiple Scattering	Approximate	Y	Y	Y	Y
Fast Running	Y	Y	Y	N	N
Ground- air- or space-based observer	All	Space	Space	All	All
Curved Earth Shadow / Twilight	Y	N	N		Y
Moon/Stars/City Lights	Y	N	N		
2-D (directional) images	Y	Y	TOA SW up (Isotropic)	Y	Y
Wavelengths	VIS	VIS + IR	VIS + IR		
Grid Resolutions	All	All	All	<=100m	All

Figure 1. Overview showing features of interest for a sampling of radiative transfer packages.

https://doi.org/10.5194/amt-2019-81
Preprint. Discussion started: 3 June 2019

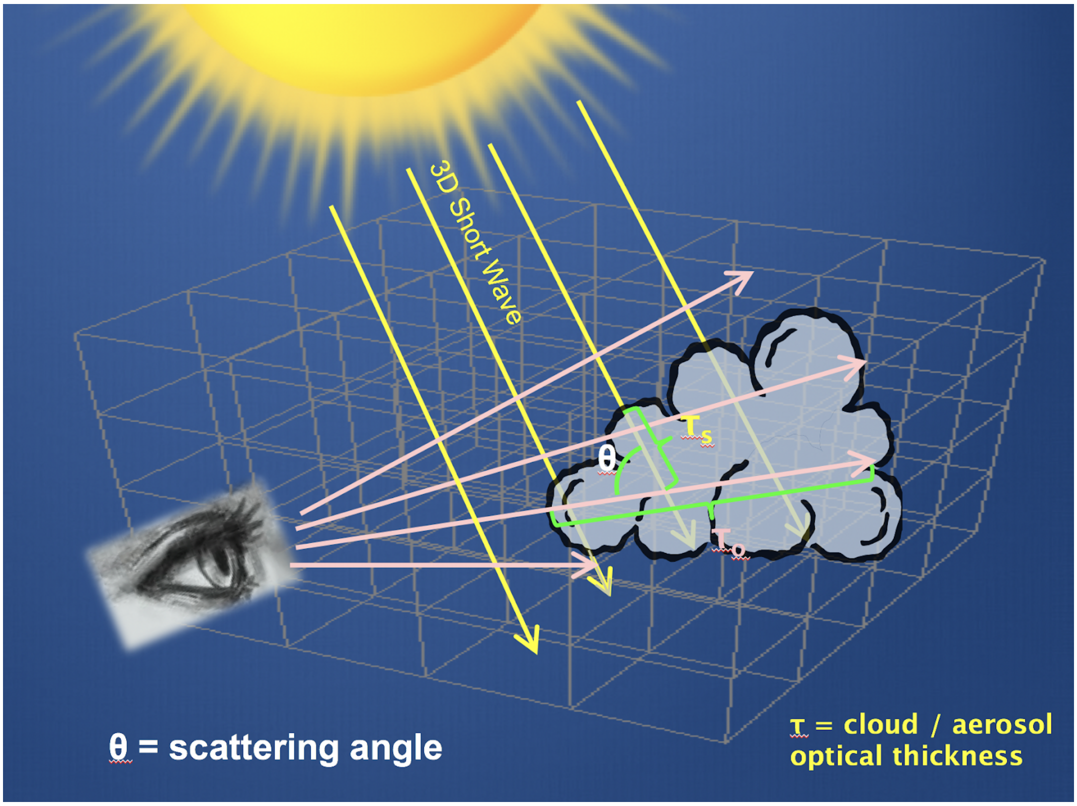

Figure 2. General ray-tracing procedure showing forward light rays (yellow) coming from the light source. A second set of light rays (pink) are traced backward from the observer. The forward and backward optical thicknesses (τ_s and τ_o) are calculated along these lines of sight and used for subsequent calculations to estimate the radiance on an angular grid as seen by the observer.

https://doi.org/10.5194/amt-2019-81
Preprint. Discussion started: 3 June 2019

Atmospheric Measurement Techniques Discussions

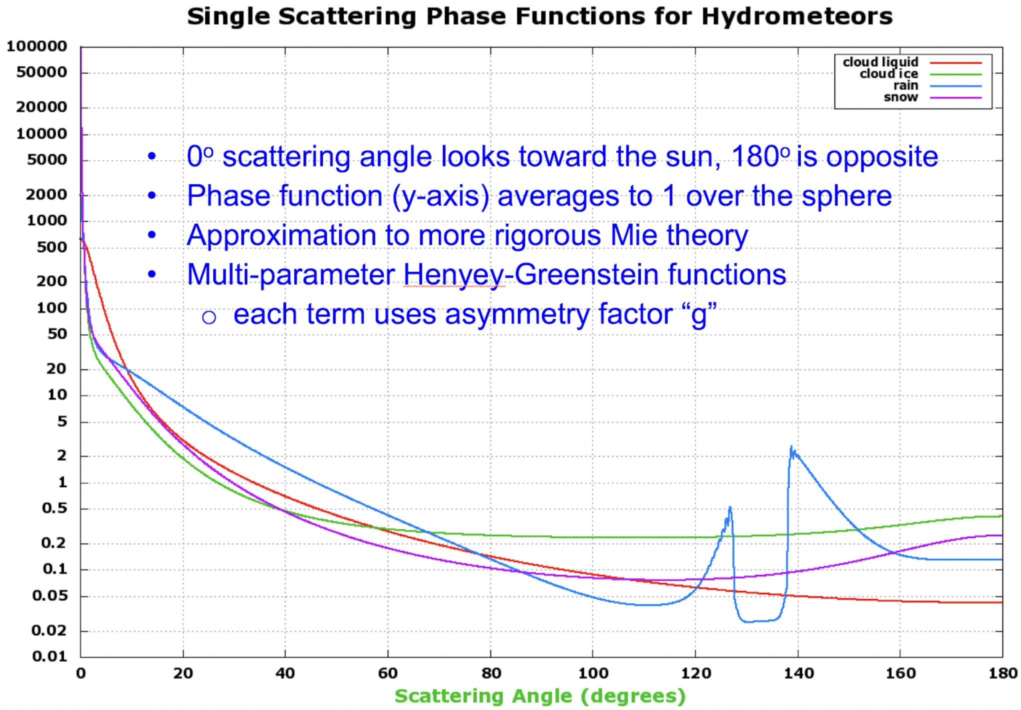

Figure 3. Single scattering phase functions used for cloud liquid, cloud ice, rain, and snow.

https://doi.org/10.5194/amt-2019-81
Preprint. Discussion started: 3 June 2019

Atmospheric Measurement Techniques Discussions
Open Access

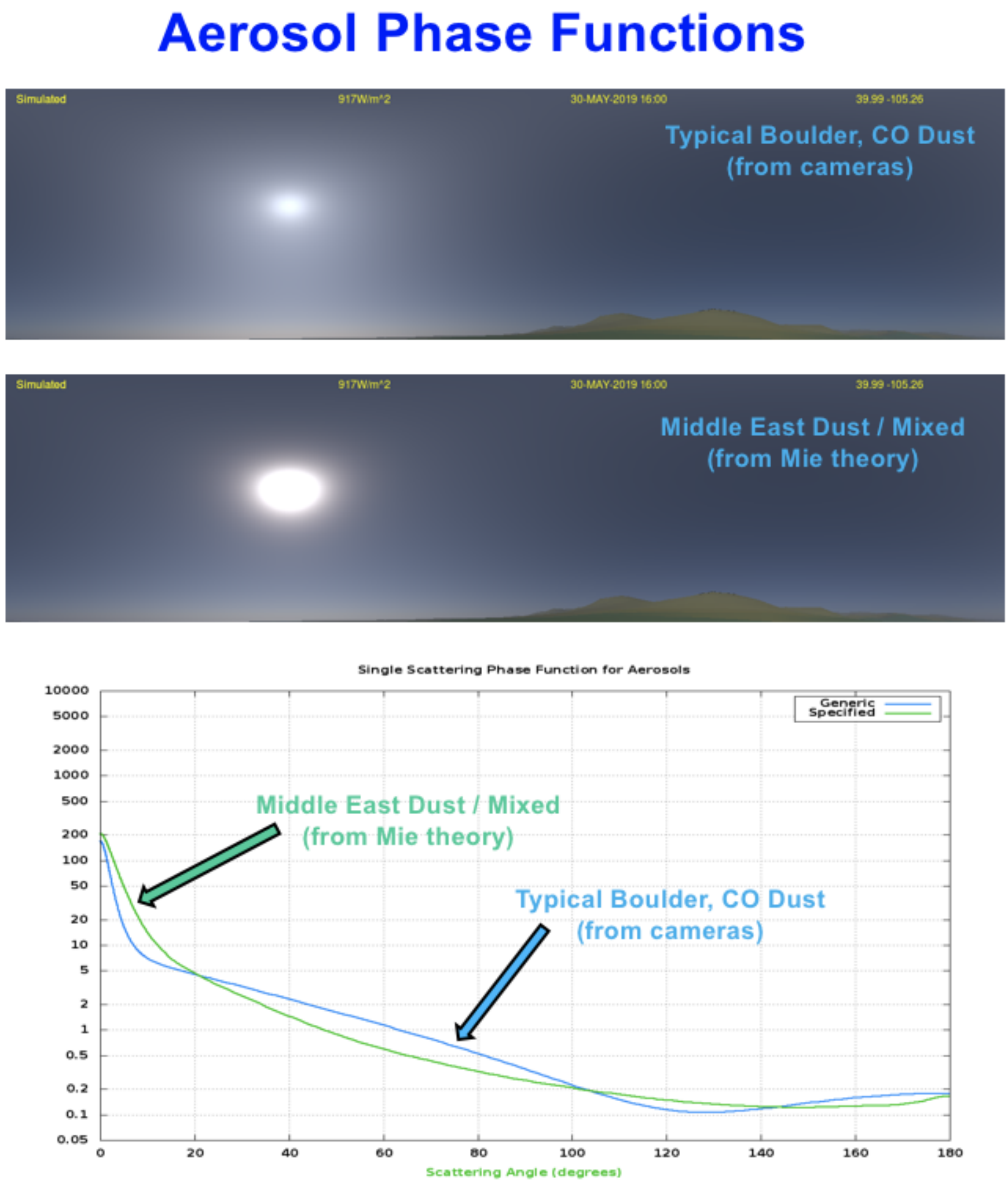

Figure 4. Simulated panoramic images with an AOD of 0.1 using the Colorado empirical phase function (a), and the Mie theory mixed dust case (b). These two phase functions are compared in (c).

https://doi.org/10.5194/amt-2019-81
Preprint. Discussion started: 3 June 2019

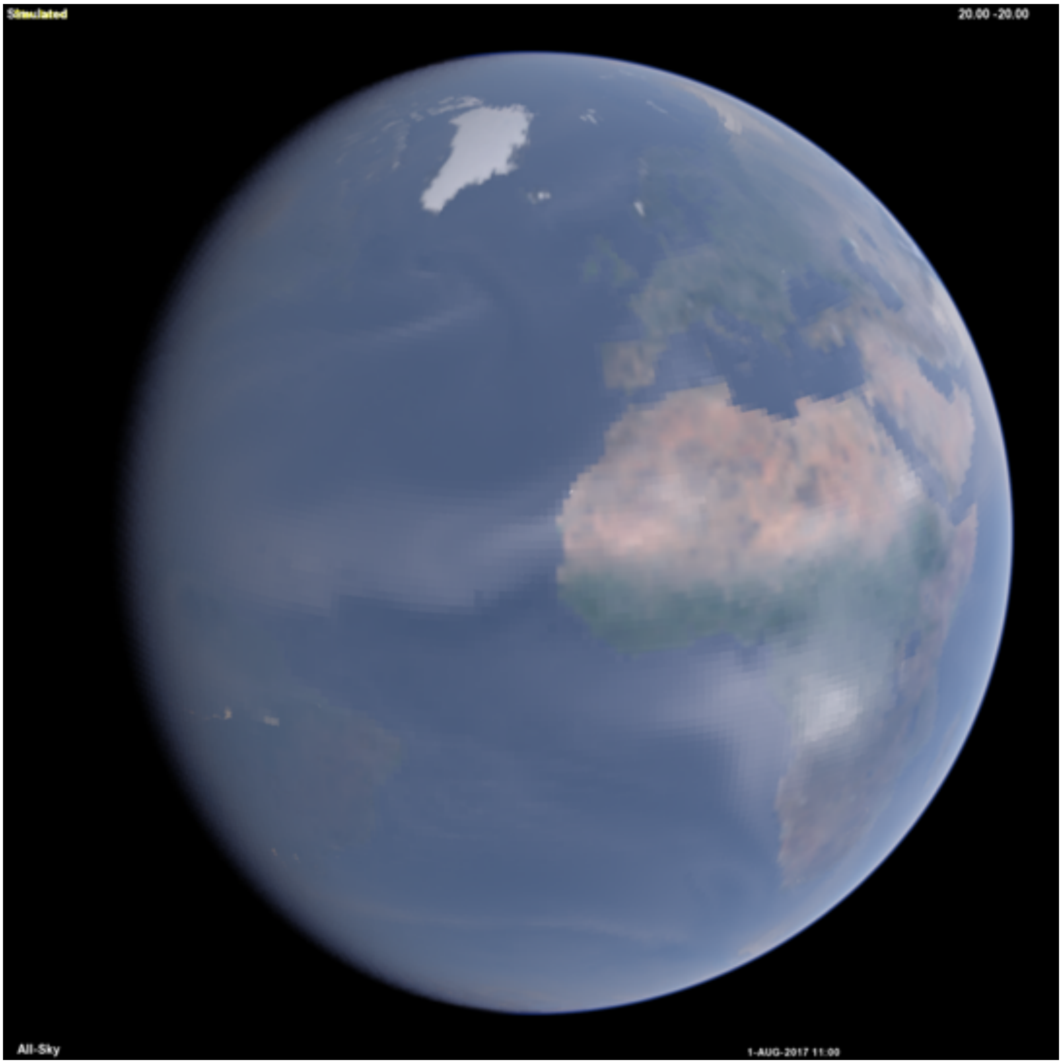

Figure 5. View from space of the NAVGEM global model, using aerosols only. The perspective point is $1.5 \times 10^6 km$ distant.

https://doi.org/10.5194/amt-2019-81
Preprint. Discussion started: 3 June 2019

Atmospheric Measurement Techniques Discussions

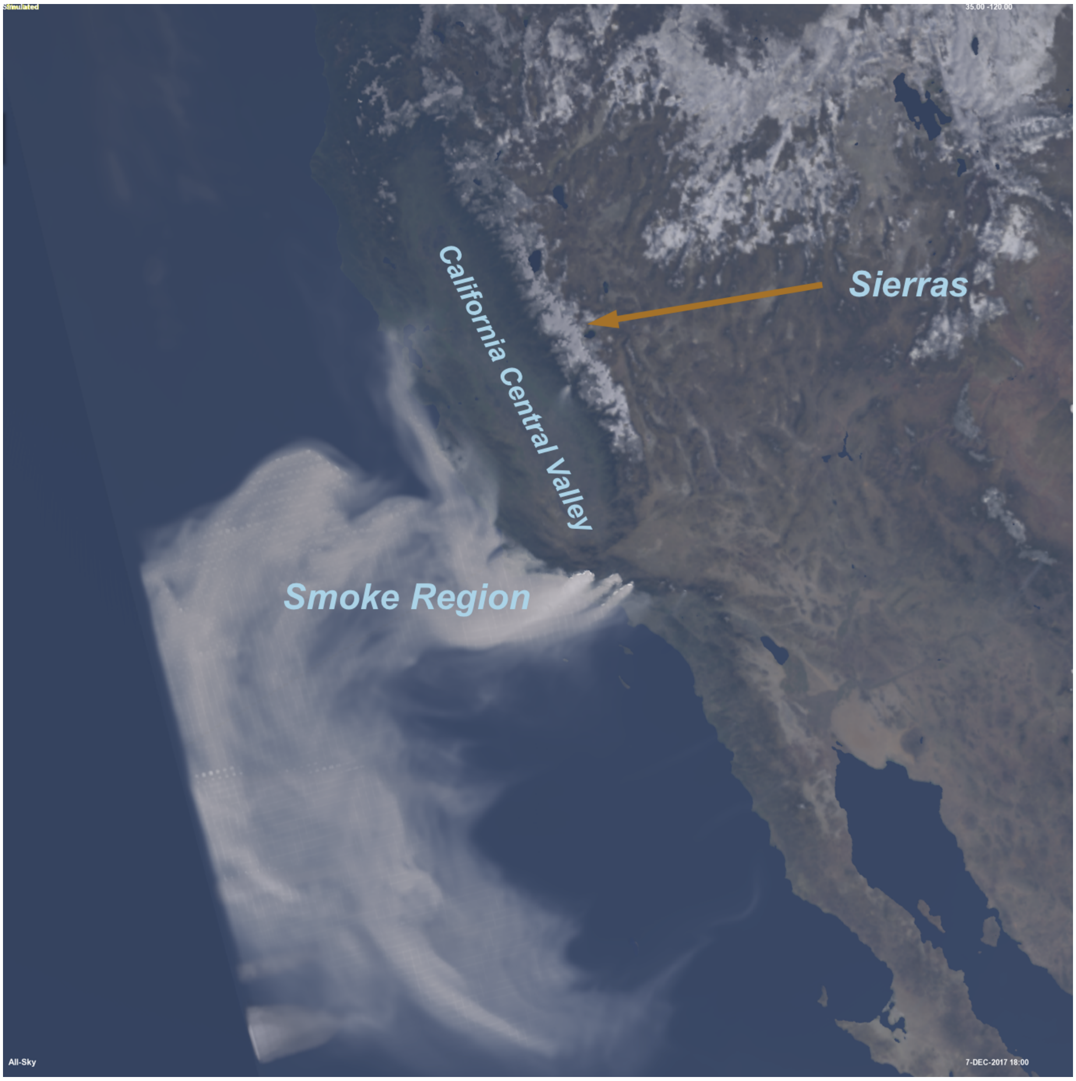

Figure 6. Simulated image of a HRRR-Smoke forecast showing the smoke plume from California wildfires during December 2017. The view is zoomed in from a perspective point at $40000\ km$ altitude.

https://doi.org/10.5194/amt-2019-81
Preprint. Discussion started: 3 June 2019

Atmospheric Measurement Techniques
Open Access
Discussions

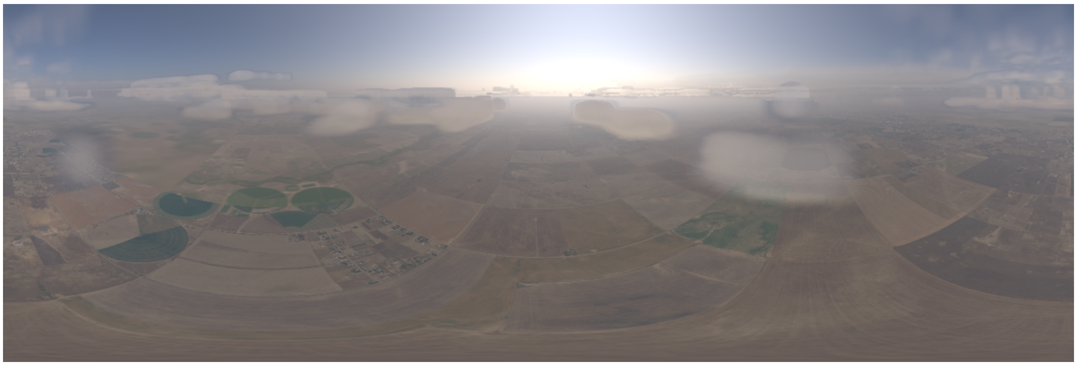

Figure 7. In-situ panoramic view in the lower troposphere showing smoke aerosols and hydrometeors. This is part of an animation simulating an airplane landing at the Denver International Airport. The panorama spans 360^o from a perspective $\sim 4km$ above ground.

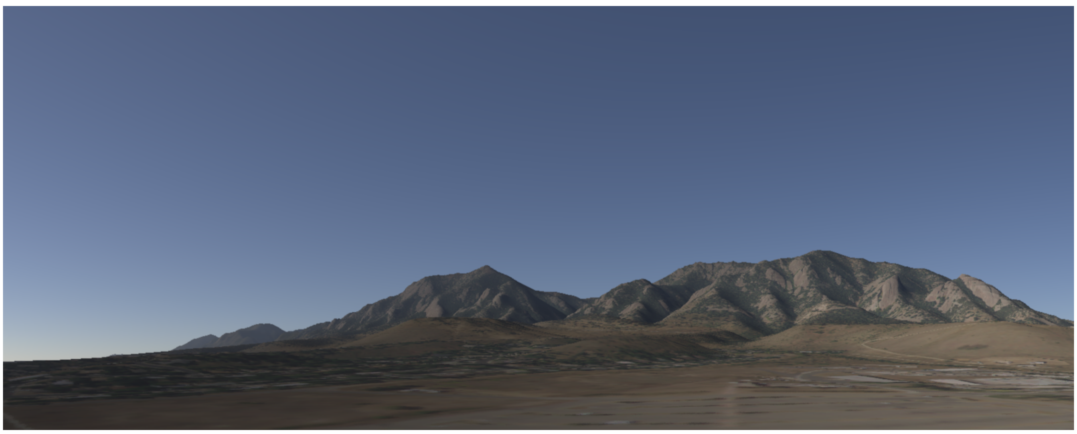

Figure 8. SWIm generated image for a hypothetical clear-sky case having a small amount of aerosols. The model grid and associated terrain data is at 30m resolution and surface spectral albedo information is derived from 0.7m resolution aerial imagery from the USDA. The vantage point is from the U.S. Department of Commerce campus in Boulder, Colorado, looking at azimuths from south through west.

https://doi.org/10.5194/amt-2019-81
Preprint. Discussion started: 3 June 2019

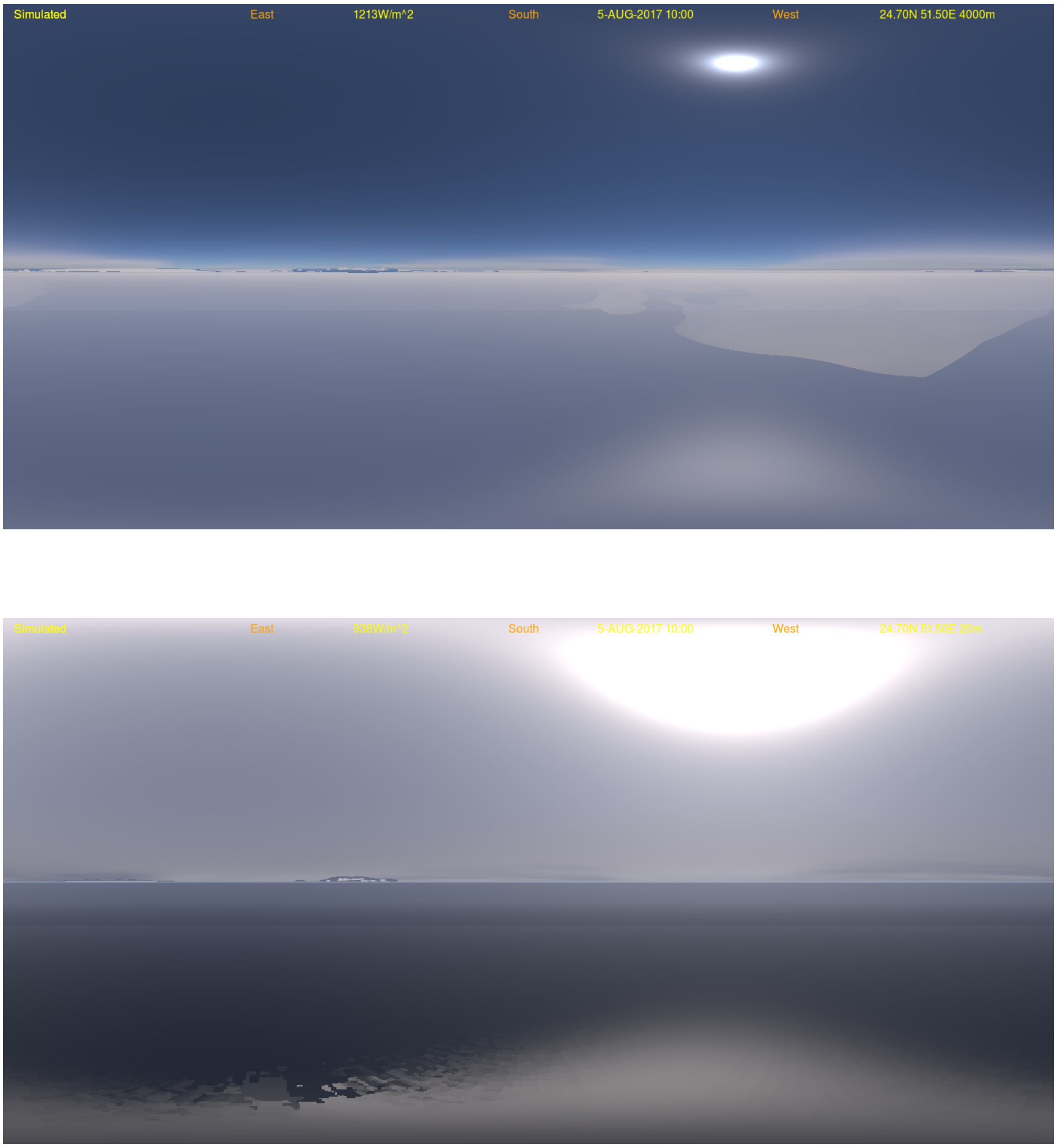

Figure 9. View (a) from $4\ km$ above the Persian Gulf of a RAMS model simulation showing dust, hydrometeors, land surface, and water including sun glint, displayed with a cylindrical (panoramic) projection. The vantage point in (b) is $20\ m$ above the water surface.

https://doi.org/10.5194/amt-2019-81
Preprint. Discussion started: 3 June 2019

Atmospheric Measurement Techniques Discussions

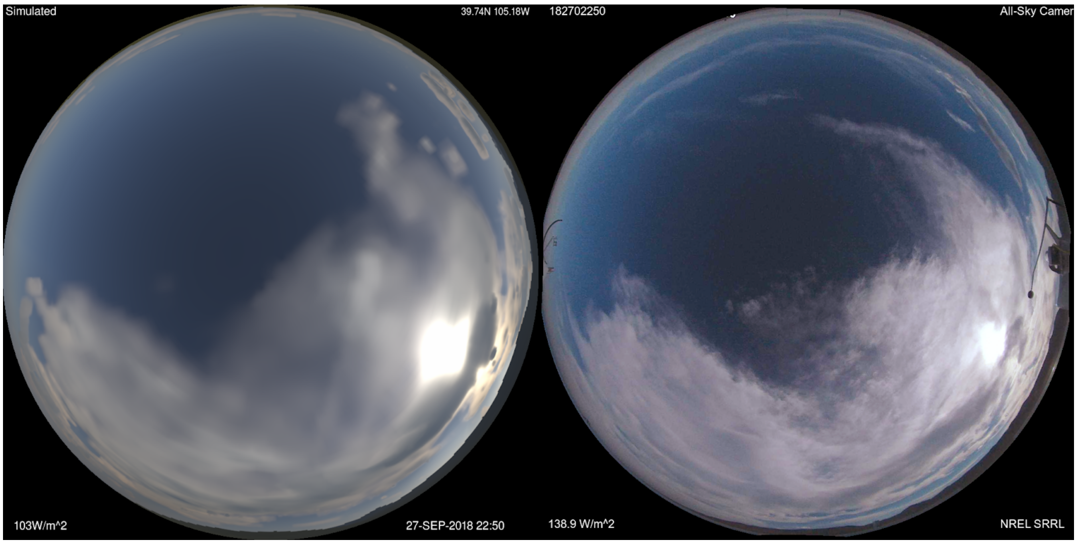

Figure 10. Comparison of observed allsky image (right) to simulated (left) over Golden, Colorado on September 27, 2018 at 2250UTC. This ground-based all-sky view is on a polar equidistant projection showing the upward looking hemisphere.

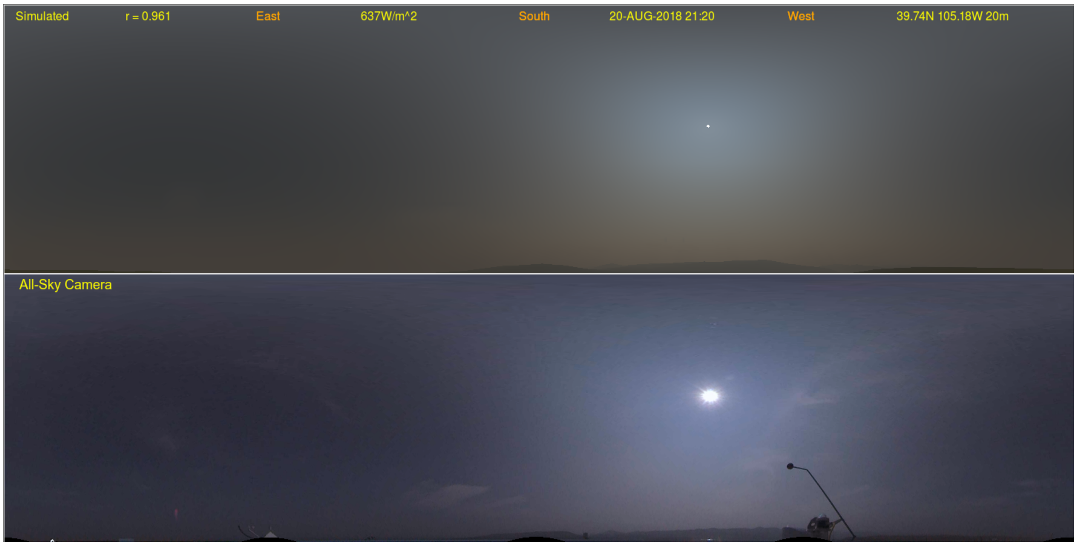

Figure 11. A comparison of aerosols at 2100UTC on August 20, 2018 in Golden, Colorado showing the simulated panoramic image (top) and all-sky camera image (bottom).

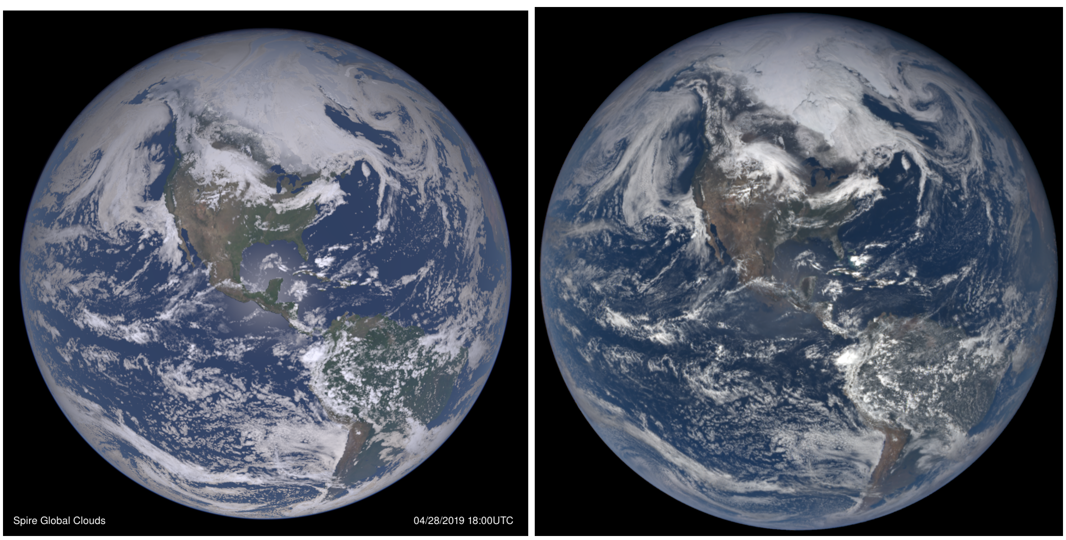

Figure 12. Side-by-side comparison (SWIm image on the left, DSCOVR-EPIC image on the right). Both images are from approximately 1800UTC on April 28, 2019.

https://doi.org/10.5194/amt-2019-81
Preprint. Discussion started: 3 June 2019

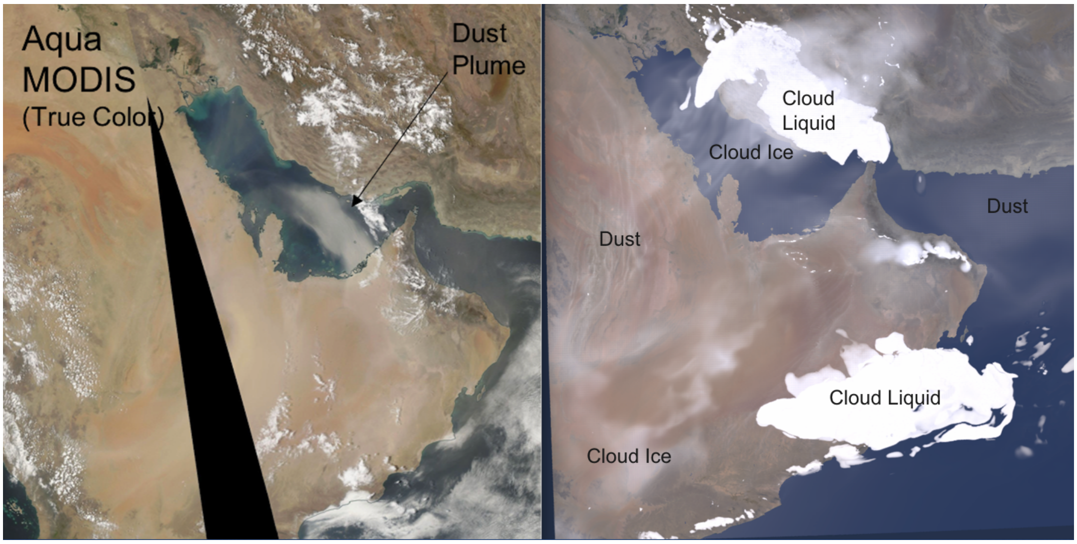

Figure 13. Aqua-MODIS image (left) taken from passes at about 1330 local time over the Arabian Peninsula compared with SWIm visualization of a RAMS model forecast (right) from 1000UTC. Areas having predominantly dust, cloud liquid, and cloud ice are annotated in the images.

https://doi.org/10.5194/amt-2019-81
Preprint. Discussion started: 3 June 2019

Appendix A.

The Arabian Peninsula case is calculated using the representative dust model derived as follows from the Capo Verde site in the AERONET network (Holben et al., 1998). We the applied EPA positive matrix factorization (PMF) 5.0 model (available at https://www.epa.gov/air-research/positive-matrix-factorization-model-environmental-data-analyses) to the dataset, using as factors the aerosol optical depth (AOD) for the fine and coarse modes and the total absorption aerosol optical depth (AAOD) from the Capo Verde site, for all Level 2.0 Inversion V3 data from 1994-2017. Two factors were derived (Figure A1). The factor with high AOD contributions from the coarse mode was flagged as the dust source. The derived absorption angstrom exponent (AAE) for Factor 1 was 4.387 for the Capo Verde site and the average extinction Ångstrom exponent (EAE) was 0.0905, lying in the range of the dust aerosol characteristics identified in Giles et al. (2012). The factor with high AAOD was believed to be associated with urban / industrial aerosols. For those samples, the averaged AAE and EAE were 0.729 and 1.164, respectively, similar to reported optical properties of absorbing fine particles (Giles et al., 2012). We selected data with corresponding PMF-identified dust source contributions larger than 95% to characterize the dust properties. The average normalized volume size distributions for the dusty days is shown in Figure A2. We used the average retrieved refractive index for the same dusty days, and the aspect ratio distribution in Dubovik et al (2006), to calculate the phase function and related optical properties used in this study.

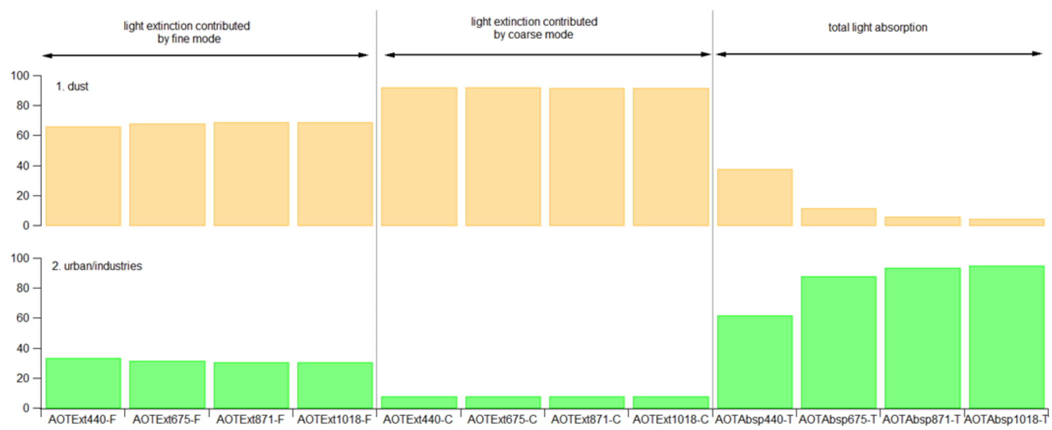

Figure A1. Optical source profile (% of species in each source) for the Capo Verde dataset.

https://doi.org/10.5194/amt-2019-81
Preprint. Discussion started: 3 June 2019

Atmospheric Measurement Techniques Discussions

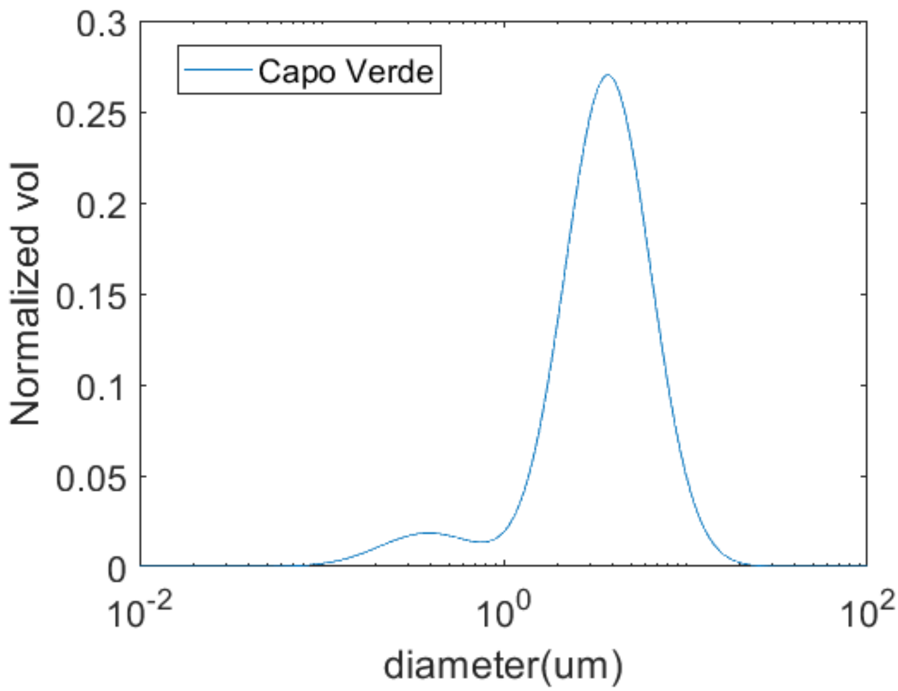

Figure A2. Average normalized volume size distribution for dust-dominated days in the Capo Verde data set.